

MUSE GAS FLOW AND WIND (MEGAFLOW) I: FIRST MUSE RESULTS ON BACKGROUND QUASARS ¹I. SCHROETTER^{2,4}, N. BOUCHÉ³, M. WENDT^{5,6}, T. CONTINI^{2,4}, H. FINLEY^{2,4}, R. PELLÓ^{2,4}, R. BACON⁷, S. CANTALUPO⁹, R. A. MARINO⁹, J. RICHARD⁷, S. J. LILLY⁹, J. SCHAYE⁸, K. SOTO⁹, M. STEINMETZ⁵, L. A. STRAKA⁸, L. WISOTZKI⁵*Draft version July 17, 2022*

Abstract

The physical properties of galactic winds are one of the keys to understand galaxy formation and evolution. These properties can be constrained thanks to background quasar lines of sight (LOS) passing near star-forming galaxies (SFGs). We present the first results of the MusE GAs FLOw and Wind (MEGAFLOW) survey obtained of 2 quasar fields which have 8 Mg II absorbers of which 3 have rest-equivalent width greater than 0.8 Å. With the new Multi Unit Spectroscopic Explorer (MUSE) spectrograph on the Very Large Telescope (VLT), we detect 6 (75%) Mg II host galaxy candidates withing a radius of 30'' from the quasar LOS. Out of these 6 galaxy-quasar pairs, from geometrical arguments, one is likely probing galactic outflows, two are classified as “ambiguous”, two are likely probing extended gaseous disks and one pair seems to be a merger. We focus on the wind–pair and constrain the outflow using a high resolution quasar spectra from Ultraviolet and Visual Echelle Spectrograph (UVES). Assuming the metal absorption to be due to gas flowing out of the detected galaxy through a cone along the minor axis, we find outflow velocities of the order of $\approx 150 \text{ km s}^{-1}$ (i.e. smaller than the escape velocity) with a loading factor, $\eta = \dot{M}_{\text{out}}/\text{SFR}$, of ≈ 0.7 . We see evidence for an open conical flow, with a low-density inner core. In the future, MUSE will provide us with about 80 multiple galaxy–quasar pairs in two dozen fields.

Subject headings: galaxies: evolution — galaxies: formation — galaxies: intergalactic medium — quasars: individual: SDSSJ213748+001220, SDSSJ215200+062516

1. INTRODUCTION

In spite of the successes of the Λ CDM cosmological model (i.e. Springel et al. 2005), a major discrepancy remains between the predicted number density of dark matter halos and the observed number density of galaxies in the low-mass regime ($L < L_*$) (i.e. Guo et al. 2010; Papastergis et al. 2012; Moster et al. 2010, 2013; Behroozi et al. 2013). This behavior is usually explained by supernova(SN)-driven outflows (Dekel & Silk 1986) which expel baryons from the galactic disk. Indeed, these galactic outflows are observed in almost every star-forming galaxy (SFG) (Veilleux et al. 2005, for a review) and are likely to enrich the inter-galactic medium (e.g. Dekel & Silk 1986; Aguirre et al. 2001; Oppenheimer & Davé 2006).

¹ Based on observations made at the ESO telescopes under programs 094.A-0211(B) and 293.A-5038(A).

² IRAP, Institut de Recherche en Astrophysique et Planétologie, CNRS, 14, avenue Edouard Belin, F-31400 Toulouse, France

³ IRAP/CNRS, 9, avenue Colonel Roche, F-31400 Toulouse, France

⁴ University Paul Sabatier of Toulouse/ UPS-OMP/ IRAP, F-31400 Toulouse, France

⁵ AIP, Leibniz-Institut für Astrophysik Potsdam, An der Sternwarte 16, D-14482 Potsdam, Germany

⁶ Institut für Physik und Astronomie, Universität Potsdam, D-14476 Golm, Germany

⁷ Univ Lyon, Univ Lyon1, Ens de Lyon, CNRS, Centre de Recherche Astrophysique de Lyon UMR5574, F-69230, Saint-Genis-Laval, France

⁸ Leiden Observatory, Leiden University, PO Box 9513, 2300 RA Leiden, The Netherlands

⁹ ETH Zurich, Institute of Astronomy, Wolfgang-Pauli-Str. 27, 8093 Zurich, Switzerland

¹⁰ AIG, Institut für Astrophysik, Universität Göttingen, Friedrich-Hund-Platz 1, D-37077 Göttingen, Germany

The physical mechanisms for driving galactic winds are complex and the cold gas could be accelerated by thermal energy injection (Springel & Hernquist 2003), by momentum injection from radiation pressure (e.g. Murray et al. 2005), by cosmic ray pressure (e.g. Booth et al. 2013; Salem & Bryan 2014) or by a combination of these mechanisms (e.g. Hopkins 2015) The wide range physical scales that describe SN explosions from Astronomical Unit (AU) to tens of kiloparsecs (kpc), are beyond the capabilities of cosmological simulations.

Hence, in most of these simulations, outflows are usually implemented with sub-grid prescriptions (e.g. Schaye et al. 2010; Oppenheimer et al. 2010; Vogelsberger et al. 2014). A popular sub-grid recipe is to let the loading factor η , i.e. the ratio between the outflow rate \dot{M}_{out} and the star-formation rate (SFR), be a function of galaxy (halo) mass or circular velocity V_c (Oppenheimer et al. 2010) such as $\eta \propto V_c^{-1}$ for momentum-driven winds and $\eta \propto V_c^{-2}$ for energy-driven winds. An alternative way to implement the collective effect of SN explosions is the (stochastic) implementation of thermal feedback, where galactic winds develop without imposing any input outflow velocity nor mass loading factor such as in the EAGLE simulations (e.g. Schaye et al. 2015), the FIRE simulations (Hopkins et al. 2014; Muratov et al. 2015), and the multi-phase scheme of Barai et al. (2015).

Given the high impact of SN feedback on galaxy formation and the wide range of mass loading factors used in numerical simulations (see the compilations in Zahid et al. 2014; Torrey et al. 2014; Schroetter et al. 2015), observational constraints are of paramount importance. Unfortunately, our knowledge on the loading factor or the mass outflow rate \dot{M}_{out} is incomplete despite of the

many efforts made in the past decades (i.e. Lehnert & Heckman 1996; Heckman et al. 2000; Martin 1998, 1999; Rupke et al. 2005; Rubin et al. 2010; Martin et al. 2012). Indeed, estimates of the ejected mass flux M_{out} using standard galaxy absorption lines (e.g. Heckman et al. 1990, 2000; Pettini et al. 2002; Martin et al. 2002; Martin 2005; Martin et al. 2012, 2013) are uncertain by orders of magnitude mainly due to the difficulty in constraining the location of the probed outflowing gas¹. Indeed, the gas responsible for the blue shifted absorption lines in galaxies could be 0.1, 1 or 10 kpc away from the host. Some recent studies have made serious attempts at determining the scaling of outflow rates with galaxy properties by setting the absorbing gas at a fixed distance (Heckman et al. 2015; Chisholm et al. 2015; Wood et al. 2015).

Background quasars can give us the minimum distance of the gas from the impact parameter b and thereby potentially yield more accurate outflow rates (Bouché et al. 2012; Kacprzak et al. 2014; Schroetter et al. 2015; Muza- hid et al. 2015). One difficulty is that it is rare for the LOS to a background quasar to pass near a star-forming galaxy. Hence, one needs to devise strategies to build large samples of galaxy-quasar pairs. Another difficulty is that background quasars can probe not only the circum-galactic medium but also the outer regions of gaseous disks and the gas near other, undetected galaxies.

In order to obtain large samples of galaxy-quasar pairs, one can select quasars around galaxies or galaxies around quasars with absorption systems. The former requires quasar follow-up observations, while the latter requires one to detect the associated galaxies. In the era of large quasar catalogs from Sloan Digital Sky Survey (SDSS), we favor the absorption selection technique combined with integral field unit (IFU) observations. Indeed, from Mg II absorption-selected quasar spectra, IFUs can detect galaxies at previously unknown impact parameters. This kind of instrument also allows us to determine geometrical and kinematic properties of galaxies in the same observation. So far, IFUs such as SINFONI allowed us to probe galaxies within 20 kpc from the quasar line of sight (at redshift around 1). With the new VLT/MUSE instrument (Bacon et al. 2006, 2009), one can now detect galaxies further away (~ 250 kpc away at $z = 1$) thanks to its field of view of 1×1 arcmin (compared to $8'' \times 8''$ for SINFONI). The large wavelength coverage of MUSE (4800Å to 9300Å) allows us to target quasar fields with multiple Mg II ($\lambda\lambda 2796, 2802$) absorption lines having redshifts from 0.4 to 1.4 for $[\text{O II}]$ ($\lambda\lambda 3727, 3729$) identification. We complement the VLT/MUSE IFU observations (which have a resolution $R \sim 2000$ or 150 km s^{-1}) with VLT/UVES follow-up high-resolution spectra of the quasars in order to study the line-of-sight kinematics with the resolution ($< 10 \text{ km s}^{-1}$) necessary for obtaining accurate constraints on outflow properties.

In this paper, we present the first results on galactic outflows from our MUSE survey. In § 2 we present the survey, the MUSE+UVES data and the data reduc-

tion. § 3 describes the sample results while § 4 presents our wind model as well as individual galaxy properties. Conclusions are then discussed in § 5.

We use the ΛCDM standard cosmological parameters: $H_0=70 \text{ km s}^{-1}$, $\Omega_\Lambda=0.7$ and $\Omega_M=0.3$.

2. THE MEGAFLOW SURVEY

2.1. Target selection strategy

Current samples of galaxy–quasar pairs for strong Mg II absorbers, as in Bouché et al. (2012); Schroetter et al. (2015); Muzahid et al. (2015) and Bouché et al. (2016), are made of a dozen pairs. Here, we seek to increase the sample size by almost an order of magnitude in order to allow for statistical analysis of the relation between the absorption properties (and ultimately wind properties such as outflow rates and loading factors) and the galaxy properties. Thanks to the multiplexing capabilities of MUSE, having a sample 80–100 pairs is now within reach using 20–25 quasar fields.

As in our previous surveys, we first select background quasar spectra with Mg II $\lambda 2796$ absorption lines. For our MusE GAs FLOW and Wind (MEGAFLOW) survey, our strategy consists in selecting multiple strong Mg II absorbers to have multiple (three, four or five) in the quasar LOS (see Figure 1) from the Zhu and Ménard catalog² (Zhu & Ménard 2013) based on the SDSS survey (Ross et al. 2012; Alam et al. 2015). These Mg II absorptions should have redshifts between 0.4 and 1.4 such that the $[\text{O II}]$ $\lambda\lambda 3727, 3729$ galaxy emission lines fall into the MUSE wavelength range (4800Å to 9300Å). These absorption lines also need to have a rest equivalent width (REW) $W_r^{\lambda 2796}$ greater than 0.8 Å because of the well-known anti-correlation between impact parameter and $W_r^{\lambda 2796}$ (Lanzetta & Bowen 1990; Steidel 1995). This limit of 0.8 Å corresponds to < 100 kpc. We also need to pay attention to where the galaxy emission lines will appear in the spectrum and try to avoid bright sky emission lines as much as possible.

The MEGAFLOW survey will consist of 20–25 quasar fields and the MUSE observations started in September 2014. In October 2014, we obtained UVES observations on the first two fields (Table 1)³. In this paper, we present the first results on these two fields towards SDSSJ213748+0012 and SDSSJ215200+0625, which have 4 Mg II absorption systems each.

2.2. Observations and data reduction

2.2.1. MUSE observations

MUSE data were taken in September 2014 in visitor mode during the first Guaranteed Time Observations (GTO) run (program ID 0.94A-0211). We first point the telescope towards a quasar and then we offset the first exposure by $\approx 4 - 5''$ in Right Ascension (RA) and Declination (Dec). Each observation was composed of four exposures of 900 seconds with a rotation of 90° between every exposure as well as small dithering ($< 1''$). This observation strategy is used in order to minimize the slice pattern which appears during image reconstruc-

¹ Furthermore, outflow rates from these low-ionization metal lines also require uncertain ionization corrections (e.g. Chisholm et al. 2016).

² This catalog can be found at http://www.pha.jhu.edu/~gz323/Site/Download_Absorber_Catalog.html

³ as Director Discretionary Time (DDT) program 293.A-5038(A)

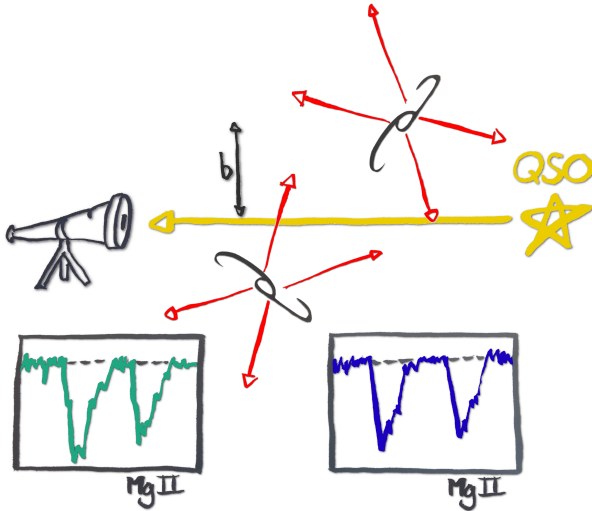


FIG. 1.— Scheme of our target selection strategy: the quasar LOS, represented by the yellow arrow heading toward the telescope, crosses two galactic outflows represented by the red arrows getting out of the galaxies. These galactic outflows absorb a portion of the quasar spectra which gives the two Mg II absorption systems at two different redshifts. b represents the impact parameter for one galaxy–quasar pair.

tion. From each MUSE observation, we obtain a combined cube of 317×316 spatial pixels (spaxels). Each spaxel has ~ 3680 spectral pixels ranging from 4750 \AA to 9350 \AA . With a spectral sampling of $1.25 \text{ \AA}/\text{pixel}$, the average spectral resolution of the data is $\sim 2.4 \text{ \AA FWHM}$. The spatial resolution for the two quasar fields is $\sim 0.8''$ FWHM with spatial sampling of $0.2''/\text{pixel}$ at 7000 \AA . The seeing constraint ($< 0.9''$) is necessary if we want to derive galaxy parameters and detect them. Indeed, galaxies at redshift ~ 1 can be small in size ($< 1.2''$) and we need the seeing to be smaller than the galaxy to better derive its parameters. Hence, low mass galaxies being faint, large-seeing diluted flux can prevent from galaxy detection (see § 3.1).

2.2.2. MUSE data reduction

The data are reduced using version 1.0 of the MUSE data reduction software (DRS) pipeline⁴. We process bias, flat field calibrations and arc lamp exposures taken during the night of the observations. Following calibration processing, raw science frames are bias subtracted and flat-fielded using master bias and master flat fields respectively. The flat-fielding is renormalized in each slice to account for slight changes due to temperature variations using a single flat field exposure taken hourly before the science observation or when the instrument temperature changes by more than 0.5° C . An additional flat-field correction was performed using the twilight sky exposures taken at the beginning of each night to correct for slight optical path differences between sky and calibration unit. Geometrical calibration and astrometric solution are then applied. The wavelength solution is obtained from the arc lamps and calibrated in air. Wavelengths are also corrected for the heliocentric velocity. The flux calibration is obtained from a spectrophotometric star observed for each night.

⁴ A short description of the pipeline is given in Weilbacher et al. (2014).

On each individual exposure, we use the default configuration of the DRS recipe and with the sky removal method turned off. This produces, for the 4 individual exposures, a large table called the “pixel-table”. For each individual exposure, star positions were registered in order to have accurate relative astrometry as shifts can occur between exposures due to the derotator wobble ($< 0.3''$). The “pixel-tables” were then combined into a single data cube using the previously calculated offsets. The sky-subtraction was performed on this combined data cube with ZAP (Zurich Atmosphere Purge), an algorithm developed by Soto et al. (2016a,b). ZAP operates by first subtracting a baseline sky level, found by calculating the median per spectral plane and then uses principal component analysis and determines the minimal number of eigenspectra that can reconstruct the residual emission features in the data cube. Absolute astrometry is obtained by matching the positions of point sources in the data cube against the SDSS astrometry.

Finally, we cross-checked the flux calibration of these point sources against the SDSS magnitudes in the r and i filter bands (the central wavelengths are $\lambda_r = 6165 \text{ \AA}$ and $\lambda_i = 7481 \text{ \AA}$ for r and i filters respectively) whose band-pass are within the MUSE wavelength coverage. Using the r and i images obtained from the MUSE data cube convolved with the SDSS filters, we fitted a Moffat profile on each of the stars to calculate their total flux in each filter and then compare them with the SDSS ones. SDSS filters are designed to be in AB magnitudes, but there are still corrections needed for some filters. Given that for the r and i filters, the AB to SDSS magnitudes correction is negligible, we can correct fluxes into AB magnitudes directly using the following relation:

$$AB = -2.5 \log_{10}(f) - 5 \log_{10}(< \lambda >) - 2.406 \quad (1)$$

where f is the flux in $\text{erg s}^{-1} \text{cm}^{-2} \text{\AA}^{-1}$ and $< \lambda >$ the filter central wavelength in \AA .

The comparison between MUSE and SDSS magnitudes is shown in Table 2. For both fields (J2137+0012 and J2152+0625), the agreement is around 1/10th of a magnitude. In addition, another data reduction was performed using CubeFix and CubeSharp (Cantalupo, in prep) in order to show cleaner images of the fields in the Appendix (Fig A.1 and A.2).

2.2.3. UVES observation and reduction

The high resolution spectra for J213748+0012 and J215200+0625 were taken with UVES mounted on the 8.2m VLT at Paranal, Chile (Dekker et al. 2000). These two fields were observed in DDT time under the program 293.A-5038(A). UVES is a cross-dispersed echelle spectrograph with two arms that are functionally identical: one covers the wavelengths in the range $3000\text{--}5000 \text{ \AA}$ (Blue) and the other covers the range $4200\text{--}11000 \text{ \AA}$ (Red). The details of the observational campaigns are presented in Table 3. The slit width of 1.2 arcsec and a CCD readout with 2×2 binning used for all the observations resulted in a spectral resolution power $R \approx 38000$ dispersed on pixels of $\sim 1.3 \text{ km s}^{-1}$. The settings were chosen in order to have a maximum of absorptions from host galaxies (from Fe II $\lambda 2586$ to Mg I $\lambda 2852$). The Common Pipeline Language (CPL version 6.3) of the UVES

TABLE 1
SUMMARY OF MUSE 094.A-0211(B) OBSERVATIONS.

Field (1)	z_{qso} (2)	PSF('') (3)	$T_{\text{exp}}(\text{s})$ (4)	Date (5)
J213748+0012	1.668	0.8	3600	2014-09-23
J215200+0625	2.409	0.7	7200	2014-09-24

(1) Quasar name; (2) Quasar emission redshift; (3) FWHM of the seeing PSF (at $\approx 7000 \text{ \AA}$); (4) Exposure time; (5) Date of observations.

TABLE 2
MAGNITUDE DIFFERENCES BETWEEN MUSE AND SDSS FOR J213748+0012 AND J215200+0625 FIELDS.

Field (1)	object (2)	Instrument (3)	RA (4)	DEC (5)	mag_r (6)	mag_i (7)	Difference (8)
J213748+0012	QSO	MUSE	21:37:48.41	+00:12:20.49	18.33	18.19	-0.13
		SDSS	21:37:48.44	+00:12:20.00	18.20	18.05	
	Star	MUSE	21:37:47.65	+00:12:21.29	19.71	19.55	-0.09
		SDSS	21:37:47.65	+00:12:20.89	19.61	19.46	
J215200+0625	QSO	MUSE	21:52:00.05	+06:25:17.26	19.42	19.44	-0.07
		SDSS	21:52:00.03	+06:25:16.36	19.42	19.30	
	Star	MUSE	21:51:59.84	+06:25:05.48	16.71	16.47	-0.17
		SDSS	21:51:59.83	+06:25:04.72	16.53	16.29	

(1) Field; (2) Object type; (3) Instrument (MUSE or SDSS); (4) Right Ascension (RA); (5) Declination (DEC); (6) Magnitude in r filter (central wavelength $\lambda_r = 6165 \text{ \AA}$); (7) Magnitude in i filter (central wavelength $\lambda_i = 7481 \text{ \AA}$); (8) Average difference SDSS–MUSE (mag).

pipeline was used to bias correct and flat field the exposures and then to extract the wavelength and flux calibrated spectra. After the standard reduction, the custom software UVES popler⁵ (version 0.66) was used to combine the extracted echelle orders into single 1D spectra. The continuum was fitted with low-order polynomials.

3. MEGAFLOW SAMPLE FIRST RESULTS

3.1. Galaxy detections

As we mentioned, the two fields (SDSSJ213748+0012 and SDSSJ215200+0625) were selected to each have at least 3 absorbing systems, and actually have 4 absorbing systems each but not all with $W_r > 0.8 \text{ \AA}$ (see Table 4).

In each MUSE field, we search for [O II] $\lambda\lambda 3727, 3729$ emission lines corresponding to the Mg II absorption redshifts seen in the quasar spectrum. However, the MUSE field of view of $1' \times 1'$ allows us to search for other companions in the fields, giving insight into the environment related to the host. We allow the potential host galaxies to have a redshift difference within a velocity interval of $\approx 1000 \text{ km s}^{-1}$ with respect to the absorber redshift ($z_{\text{gal}} = z_{\text{abs}} \pm 0.01$ for a $z \approx 1$ galaxy). This velocity interval is set to prevent selection effects on surrounding gas velocities and thus not rejecting gas able to escape the gravitational well of the host galaxy in case of outflowing gas (more details on escape velocity in § 4.2). In the case where there are multiple galaxy candidates for a single Mg II line, we select the galaxy with the smallest impact parameter from the quasar LOS. Table 4 shows the detection rates for each field. For one of the undetected galaxies the expected emission line falls near a sky emission line at 7618 \AA (the $z \approx 1.0437$ absorber in SDSSJ213748+0012) and the other line is too faint to be detected. For the reader interested in all of the galaxies detected in these MUSE data, we provide in the appendix a catalog with all the galaxies for which a redshift could be determined.

We detect galaxies at redshifts of three of the four

Mg II absorbers for the SDSSJ213748+0012 quasar field (see Table 4). For the Mg II absorber at $z = 0.8063$, we find one [O II] emission-line galaxy at a distance b of 88 kpc. For the $z = 1.1890$ Mg II absorber, we also find one galaxy at an impact parameter of 63 kpc. For the last $z = 1.2144$ Mg II absorber, we find three [O II] emitters, at impact parameters of 87, 212 and 246 kpc. Given the large impact parameters of the latter two galaxies compared to the typical galaxy halo at these redshifts, and given the large Mg II REW of 1 \AA , we assume the galaxy with the smallest impact parameter to be the host galaxy.

For the SDSSJ215200+0625 field, we also detect galaxies at the redshifts of three out of the four Mg II absorbers (see Table 4). Two galaxies are identified for the first Mg II absorber at $z = 1.0534$, at impact parameters of 45 and 189 kpc. The host of the second absorber at $z = 1.1761$ is not detected in spite of the wavelength for the expected [O II] line being clear of OH lines. The third Mg II absorption has a redshift of 1.3190 and has only one galaxy corresponding to that redshift at an impact parameter of 34 kpc. The last Mg II absorption is at $z = 1.4309$ and we found 4 [O II] emitters at that redshift, which have impact parameters of 62, 78, 184 and 211 kpc. This is indicative of a group environment. Out of these 4 galaxies, two have impact parameters very close to each other (62 and 78 kpc). We choose to assume that the closest galaxy (at 62 kpc) should be responsible for the Mg II absorption.

Using the propagated noise in the MUSE datacube, we can estimate flux (and surface brightness) limits on the expected [O II] emission line for the non-detected host galaxies. For the SDSSJ213748+0012 quasar field, at the first expected [O II] wavelength ($\sim 6730 \text{ \AA}$), with a noise of $2.3 \times 10^{-20} \text{ erg s}^{-1} \text{ cm}^{-2} \text{ \AA}^{-1}$ (1σ), we estimate a surface brightness limit of $1.43 \times 10^{-18} \text{ erg s}^{-1} \text{ cm}^{-2} \text{ arcsec}^{-2}$ (1σ) for emission line objects (assuming a FWHM = 2.48 \AA). This corresponds to a flux limit of $1.04 \times 10^{-18} \text{ erg s}^{-1} \text{ cm}^{-2}$ (1σ) for an unresolved emitter at $0.82''$ see-

⁵ http://astronomy.swin.edu.au/~mmurphy/UVES_popler/

TABLE 3
SUMMARY OF UVES 293.A-5038(A) OBSERVATIONS.

Target	setting λ_c (nm)	T_{exp} (s)	Date
J213748+0012	390+580	5970	2014-10-19
J215200+0625	390+580	9015	2014-10-21,24 2014-11-18

TABLE 4
SUMMARY OF MUSE GALAXY DETECTION.

Field name	z_{absorber}	$W_r^{\lambda 2796}$	N_{det}	b
(1)	(2)	(3)	(4)	(5)
J213748+0012	0.8063	0.724 ± 0.09	1	88
	1.0437	0.767 ± 0.08	0 ^a	...
	1.1890	0.308 ± 0.06	1	63
	1.2144	1.144 ± 0.06	3	87, 212, 246
J215200+0625	1.0534	0.522 ± 0.14	2	45, 189
	1.1761	0.526 ± 0.15	0	...
	1.3190	1.347 ± 0.12	1	34
	1.4309	1.152 ± 0.11	4	62, 78, 184, 211

(1) Quasar field name; (2) Mg II absorption lines redshift; (3) Mg II ($\lambda 2796$) REW (Å); (4) Number of detected galaxies near absorber redshift; (5) Impact parameter(s) of the detected galaxy(ies) (kpc);

^aAffected by OH emission line at 7618Å. The flux limit is $\sqrt{2}$ times for the [O II] doublet (assuming a resolved doublet), or 1.47×10^{-18} ergs $^{-1}$ cm $^{-2}$ (1σ), which corresponds to a SFR of 0.13 M $_{\odot}$ yr $^{-1}$ at $z = 1$, typical of our sample. Surface brightness and flux limits are shown in Table 5.

3.2. SFR determination

We use the $L_{\text{O II}}$ ($\lambda\lambda 3727, 3729$) luminosity to estimate the SFR as follows. First, we use the Kennicutt (1998) calibration, which assumes a Salpeter (1955) Initial Mass Function (IMF):

$$\text{SFR}(\text{M}_{\odot} \text{ yr}^{-1}) = (1.4 \pm 0.4) \times 10^{-41} L_{\text{O II}}(\text{erg s}^{-1}) \quad (2)$$

Using a Chabrier (2003) IMF and assuming a mean flux attenuation of $A_V = 1$, which is typical for $z = 1$ galaxies (e.g. Charlot et al. 2002), gives the same results (within 10%) as Equation 2. Equation 4 in Kewley et al. (2004, hereafter K04) uses also a Salpeter IMF but makes no assumption of reddening. In their paper, they show that using the “average” attenuation correction of 0.3 mag leads to underestimate the high SFR[O II] ($> 1\text{M}_{\odot} \text{ yr}^{-1}$) and overestimate the low SFRs. They provide a way of deriving the E(B-V) (Eq.16 and 18 of K04) color excess which leads to a more accurate mean attenuation, assuming that $A_V = 3.1 \times E(B - V)$. We choose to use this method to derive our SFRs.

3.3. Galaxy morpho-kinematic properties

Before classifying the galaxy–quasar pairs as favorable for gas outflows or inflows based on the azimuthal angle α of the apparent quasar location with respect to the galaxy major axis, we need to determine the galaxy’s major axis position angle (PA) (see Figure 2).

We determine the PAs from the morpho-kinematic properties of each galaxy using two approaches. First, we used the 2D fitting tool Camel⁶ on the [O II] emission lines to extract velocity and dispersion maps as in

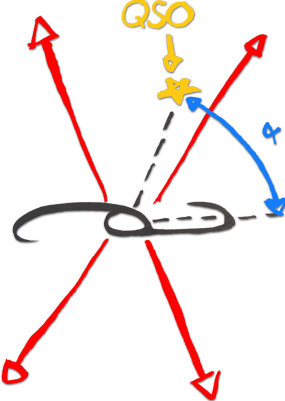


FIG. 2.— Scheme representing the azimuthal angle: The galaxy is represented at the center in black, the red arrows represent the outflowing gas expelled from both side of the galaxy minor axis. The azimuthal angle α is represented by the blue angle between the galaxy major axis and the quasar LOS (in yellow).

Epinat et al. (2012) in order to establish whether the galaxy has a regular velocity field compatible with a disk. Second, we use the GalPaK^{3D} algorithm (Bouché et al. 2015) to derive simultaneously the morphological and kinematic properties of these galaxies using the continuum subtracted sub-cubes extracted around the [O II] emission lines. GalPaK^{3D} uses a disk parametric model with 10 free parameters and a Monte-Carlo Markov Chain (MCMC) algorithm with non-traditional sampling laws in order to efficiently probe the parameter space. Because the algorithm uses a 3-dimensional kernel to convolve the model with the spatial point-spread function (PSF or seeing) and the instrument line spread function (LSF), it returns the intrinsic (free of the PSF) galaxy properties (such as half-light radius, inclination, and maximum velocity). Other parameters include the major-axis position angle, the galaxy flux, position, redshift and intrinsic velocity dispersion. Results on the geometrical and kinematic properties of each galaxy are presented in Table 6.

Figures 3–8 show GalPaK^{3D} reconstructed models as well as Camel velocity maps for the 6 galaxies in the two fields. In Figure 3 (SDSSJ213748+0012 field), the other emission sources are the quasar and a star’s residual continuum. In these figures, the left panel corresponds to a narrow band image of 30 pixels (37.5 Å) around the galaxy’s [O II] emission lines. The background continuum has been subtracted so that we can only see the galaxy in emission. In each of these Figures, we see the galaxy (inside the white rectangles) within 15'' of the quasar LOS (represented by a white cross). In the right columns of these Figures, [O II] integrated flux and velocity maps are shown. The top row corresponds to a 2×2 (2 pixels FWHM) spatial Gaussian smoothed flux map (left) and the Camel velocity map (right). The bottom row shows the GalPaK^{3D} model flux (left) and velocity (right) maps. We can see that in

⁶ The source code can be found at <https://bitbucket.org/bepinat/camel.git>

TABLE 5
SURFACE BRIGHTNESS AND FLUX LIMITS.

Quasar field (1)	z_{absorber} (2)	LSF (3)	Noise (4)	PSF (5)	Surface brightness limit (6)	[O II] flux limit (7)
J213748+0012G1	0.8063	2.48	2.3×10^{-20}	0.82	1.43×10^{-18}	1.47×10^{-18}
J213748+0012	1.0437	2.37	3.7×10^{-20}	0.78	2.19×10^{-18}	2.14×10^{-18}
J213748+0012G2	1.1890	2.57	2.4×10^{-20}	0.75	1.54×10^{-18}	1.45×10^{-18}
J213748+0012G3	1.2144	2.43	2.4×10^{-20}	0.76	1.45×10^{-18}	1.39×10^{-18}
J215200+0625G1	1.0534	2.28	2.1×10^{-20}	0.67	1.19×10^{-18}	1.01×10^{-18}
J215200+0625	1.1761	2.60	1.7×10^{-20}	0.66	1.10×10^{-18}	9.14×10^{-19}
J215200+0625G2	1.3190	2.41	3.6×10^{-20}	0.66	2.17×10^{-18}	1.79×10^{-18}
J215200+0625G3	1.4309	2.60	2.1×10^{-20}	0.66	1.36×10^{-18}	1.13×10^{-18}

(1) Quasar field name; (2) Mg II absorption line redshift; (3) Line Spread Function FWHM (LSF) of the MUSE data (\AA); (4) Data cube noise at the expected [O II] wavelength ($\text{erg s}^{-1} \text{cm}^{-2} \text{\AA}^{-1}$) given at 1σ ; (5) PSF of the data (''); (6) Surface brightness limit ($\text{erg s}^{-1} \text{cm}^{-2} \text{arcsec}^{-2}$) given at 1σ ; (7) [O II] flux limit ($\text{erg s}^{-1} \text{cm}^{-2}$) given at 1σ .

all cases, except in Figure 4 for the dispersion-dominated SDSSJ213748+0012G2 galaxy, the model flux maps from GalPaK^{3D} is in a good agreement with the observed flux, and that GalPaK^{3D} and Camel velocity maps are consistent. Table 6 lists the resulting parameters for each galaxy.

GalPaK^{3D} results are reliable if the central galaxy pixel has, at minimum, a Signal to Noise Ratio (SNR) pixel^{-1} of 3 (Bouché et al. 2015). For each galaxy, we have SNR pixel^{-1} of 11.0, 11.0, 4.5, 9.3, 4.2, 10.5 for SDSSJ213748+0012G1, G2, G3 and SDSSJ215200+0625G1, G2, G3 respectively. We checked that the parameters have converged for each galaxy as well as cross checked on raw data whether the values for position angles and maximum rotational velocities are consistent.

3.4. Classification and notes on the individual cases

To put constraints on galactic outflows, we first need to select galaxy–quasar pairs suitable for wind studies (wind pairs). To do so, we measure the angle between the galaxy major axis and the apparent quasar location, which is referred to as the azimuthal angle α . Depending on this angle, the quasar LOS is likely to probe different phenomena around the galaxy. If $60^\circ \leq \alpha \leq 90^\circ$, the quasar’s position on the sky is roughly along the galaxy minor axis and is likely to cross the outflowing material of the galaxy (e.g. Bordoloi et al. 2011, 2014). If a pair has such an azimuthal angle, it will be classified as a wind-pair. On the other hand, if the quasar is positioned along the galaxy major axis ($0^\circ \leq \alpha \leq 30^\circ$), the quasar LOS is likely to probe inflowing or circum-galactic gas. With such configuration, we classify the pair as suitable for accretion studies (inflow pair). In between, ($35^\circ \leq \alpha \leq 55^\circ$), we cannot distinguish between these two extreme cases.

The first detected galaxy (‘G1’) in the SDSSJ213748+0012 quasar field (Figure 3) has an impact parameter $b \approx 88$ kpc and corresponds to the $z_{\text{abs}} \approx 0.8063$ Mg II absorption lines with a REW $W_r^{\lambda 2796}$ of 0.789 \AA . This J213748+0012G1 galaxy is inclined by $i \approx 49 \pm 1.4^\circ$ and its derived maximum rotation velocity is $V_{\text{max}} \approx 127 \pm 5 \text{ km s}^{-1}$. With an [O II] integrated flux of $8.7 \times 10^{-17} \text{ erg s}^{-1} \text{cm}^{-2}$, its SFR is $\approx 6.3 \pm 0.7 \text{ M}_\odot \text{ yr}^{-1}$. In Figure 3, we can see that the morphology and the position angle is well reproduced by GalPaK^{3D}. The azimuthal angle α with the quasar LOS is $\alpha = 25$ deg, i.e. the LOS is aligned with the

major-axis.

The galaxy J213748+0012G2 (Figure 4) corresponding to the $z_{\text{abs}} \approx 1.1890$ Mg II absorption lines with a REW $W_r^{\lambda 2796}$ of 0.308 \AA in the J213748+0012 quasar spectrum, has an impact parameter of $b \approx 64$ kpc and a total [O II] doublet flux of $1.47 \times 10^{-16} \text{ erg s}^{-1} \text{cm}^{-2}$. From the [O II] integrated flux we derive a SFR of $\approx 41 \pm 8.0 \text{ M}_\odot \text{ yr}^{-1}$. This galaxy has a large velocity dispersion $\sigma \approx 114 \pm 2.3 \text{ km s}^{-1}$, i.e. it is a dispersion dominated system with $V/\sigma \sim 0.2$. Furthermore, the velocity field derived from the line fitting algorithm Camel does not agree with its morphology, i.e. its morphological and kinematic main axes are strongly misaligned, by $\approx 80^\circ$ (Figure 4). This is a strong indication for a merger, and therefore this galaxy will not be considered as a wind case since the position angle of this galaxy is ambiguous.

The other galaxy (J213748+0012G3, Figure 5) from the J213748+0012 field corresponding to the Mg II absorption lines at redshift $z_{\text{abs}} \approx 1.2144$ and a REW $W_r^{\lambda 2796}$ of 1.144 \AA has an impact parameter b of ≈ 87 kpc. This galaxy has an inclination $i \approx 40 \pm 5^\circ$, a maximum rotational velocity $V_{\text{max}} \approx 166 \pm 18 \text{ km s}^{-1}$ and an [O II] flux of $4.17 \times 10^{-17} \text{ erg s}^{-1} \text{cm}^{-2}$. From this flux we derive a SFR of $\approx 8.9 \pm 1.1 \text{ M}_\odot \text{ yr}^{-1}$. Contrary to J213748+0012G2, the kinematic and morphological PAs agree well (Figure 5), hence the 3D GalPaK^{3D} model accounts for the 3D emission of this galaxy. In this case, the quasar LOS is at $\approx 45^\circ$ from the major axis of this galaxy, this pair is thus classified as ambiguous.

The first detected galaxy from the SDSSJ215200+0625 quasar field corresponds to the Mg II absorption lines at redshift $z_{\text{abs}} \sim 1.0534$ with a REW $W_r^{\lambda 2796}$ of 0.545 \AA . This galaxy (J215200+0625G1) has an impact parameter $b \approx 45$ kpc, a maximum rotational velocity $V_{\text{max}} \approx 161 \pm 2 \text{ km s}^{-1}$ and an inclination $i \approx 69 \pm 0.7^\circ$. With an [O II] integrated flux of 1.09×10^{-16} we derive a SFR of $\approx 19.0 \pm 3.1 \text{ M}_\odot \text{ yr}^{-1}$. For this galaxy, Figure 6 shows a good agreement between GalPaK^{3D} and Camel flux and velocity maps. We can clearly see that the quasar LOS is aligned with the major axis of this galaxy with $\alpha = 4$ deg and is thus classified as an inflow-pair.

The galaxy (J215200+0625G2) corresponding to the redshift $z_{\text{abs}} \approx 1.3190$ Mg II absorption lines with a rest equivalent width $W_r^{\lambda 2796}$ of 1.424 \AA has an impact parameter $b \approx 34$ kpc. The derived galaxy redshift is 1.31845 with an inclination of $i \approx 59 \pm 11^\circ$ and a maximum rotational velocity $V_{\text{max}} \approx 130 \pm 29 \text{ km s}^{-1}$. With

an [O II] flux of $\approx 1.99 \times 10^{-17}$ erg s $^{-1}$ cm $^{-2}$, we derive a SFR of $\approx 4.6 \pm 0.4$ M $_{\odot}$ yr $^{-1}$. Even if this galaxy is faint, as seen in Figure 7, its GalPaK^{3D}-derived morphology and position angle are in good agreement with Camel maps. The quasar LOS is aligned with the minor axis of this galaxy with $\alpha = 88 \pm 5$ deg.

The last galaxy (J215200+0625G3) in the J215200+0625 quasar field has an impact parameter $b \approx 63$ kpc and corresponds to the Mg II absorption lines at redshift $z_{\text{abs}} \approx 1.4309$ with $W_r^{\lambda 2796} = 1.152$ Å. The galaxy has an inclination of $i \approx 13 \pm 4$ °, a maximum rotational velocity $V_{\text{max}} \approx 298 \pm 40$ km s $^{-1}$ and an [O II] integrated flux of $\approx 5.05 \times 10^{-17}$ erg s $^{-1}$ cm $^{-2}$. With this flux we derive a SFR of $\approx 19 \pm 3.0$ M $_{\odot}$ yr $^{-1}$. Figure 8 shows that the morphology is in agreement with Camel but the position angle derived for this galaxy is more uncertain due to the low inclination of this galaxy. With an azimuthal angle of $\alpha = 72 \pm 20$ deg, we cannot determine whether the quasar LOS is aligned with the minor or major axis of the galaxy.

In addition to the azimuthal angle, if a galaxy has a low inclination, classification can be ambiguous given that the uncertainty on the position angle will be large. Figure 9 shows galaxy inclination as a function of quasar azimuthal angle. From the 5 detected galaxies in the two quasar fields that are non-mergers, 2 are classified as inflow-pairs, one is an ambiguous case as its azimuthal angle is 47°, one is a face-on galaxy and only 1 (J215200+0625G2) can be robustly classified as a wind-pair.

3.5. UVES data analysis

For each quasar spectrum, we calculate the REW for the Mg II absorption lines ($W_r^{\lambda 2796}$) in the UVES data and compare them with the SDSS calculated $W_r^{\lambda 2796}$ (see Table 7). We find that the results are consistent with each other. We also calculate REWs of the Mg II $\lambda 2803$, Mg I $\lambda 2852$, Fe II $\lambda 2586$ and Fe II $\lambda 2600$ in UVES quasar spectra. Results are shown in Table 7. Figures 10 and 11 show the UVES MgI $\lambda 2852$, Mg II $\lambda \lambda 2796, 2802$ and Fe II $\lambda \lambda 2586, 2600$ absorption profiles and label the calculated REW of each profile for both quasar fields.

One of the first deductions we can make from Figures 10 and 11 is that there is no clear difference (like different asymmetry behavior for instance) between what seems to be outflowing material and circum-galactic or inflowing gas concerning the different absorption lines.

Figure 12 shows the distribution of REW $W_r^{\lambda 2796}$ for pairs with an azimuthal angle $\alpha > 45$ ° as a function of impact parameter b for this work as well as Kacprzak et al. (2011b,a) and Schroetter et al. (2015). This Figure shows that for wind pairs, as mentioned in Bouché et al. (2012), we clearly see a tight correlation between $W_r^{\lambda 2796}$ and b . This $W_r^{\lambda 2796} - b$ correlation goes approximatively as b^{-1} . This figure shows that the anti-correlation between impact parameter b and W_r is again confirmed at $b < 100$ kpc. The scatter around the relation in Figure 12 is ≈ 0.3 dex (delineated with the dotted lines). The solid line traces the fiducial $1/b$ relation for mass-conserved bi-conical outflows (see Bouché et al. 2012).

4. WIND MODEL

In this section, we describe the wind modeling. We create a cone having an opening angle corresponding to θ_{max} (usually around 30°) and fill it randomly with particles representing cold gas clouds being pushed away by a hot medium or radiation pressure. These particles are distributed such that their number goes like $1/r^2$, where r is the distance to the galaxy center. The particle density is normalized arbitrarily to reproduce the optical depth of the absorption profiles.

Such entrained clouds are accelerated to their terminal velocity quickly in a few kpc or < 10 kpc since the pressure from the hot medium or the radiation field scales as $1/r^2$. The range of impact parameters for the galaxy–quasar pair in our sample is always larger than 30 kpc. Hence, we assume, for simplicity, that the particles have a constant radial velocity corresponding to V_{out} . In addition, a single LOS probes a rather small range of distances from the host galaxy such that a gradient in the outflow velocity would have no significant impact on our results. So far, only in one LOS with an impact parameter less than 10 kpc in Schroetter et al. (2015), we required an accelerated wind profile.

We then orient the cone following the galaxy inclination and simulate the quasar LOS such that the galaxy–quasar pair matches the geometrical configuration of the MUSE data.

The particle velocities are then projected along the simulated quasar LOS and the distribution of the projected velocities gives us a simulated optical depth τ_v , which we turn into an absorption profile $\propto \exp(-\tau_v)$. In order to facilitate comparison with the data, Poisson noise is added to the simulated absorption profile to simulate the instrumental noise. This noise is chosen to have the same level as the data.

We derive V_{out} and θ_{max} by changing their values when matching the UVES data by eye. These two parameters are independent, since V_{out} changes the outer part of the simulated profile and θ_{max} the inner part. The outer part of the profile corresponds to the furthest end of the absorption from the systemic velocity, the inner being the closest.

The best-fit model is found “by hand” and errors on these parameters are given at 1σ , assuming a gaussian noise distribution for our simulated profile. “By hand” means that we generate 10th of simulated profiles and choose by eye the one which reproduces best the data. The galaxy inclination has the same behavior as θ_{max} but since this parameter is fixed by GalPaK^{3D}, only θ_{max} is changed to fit the data for the inner part of the absorption profile.

Examples on how the wind model behaves as we change the different parameters can be seen in the appendix of Schroetter et al. (2015).

4.1. The wind–pair case of J215200+0625G2

The bottom right panel of Figure 13 shows the UVES Fe II $\lambda 2586$ absorption lines corresponding to the J215200+0625G2 galaxy redshift of $z = 1.3184$. This absorption is the one we intend to fit in order to constrain outflow properties since other absorption lines like Mg II are saturated (see middle panel of Figure 11). In this profile, we can see a “gap” of absorption around 80 km s $^{-1}$. We first tried to fit this absorption with our wind model

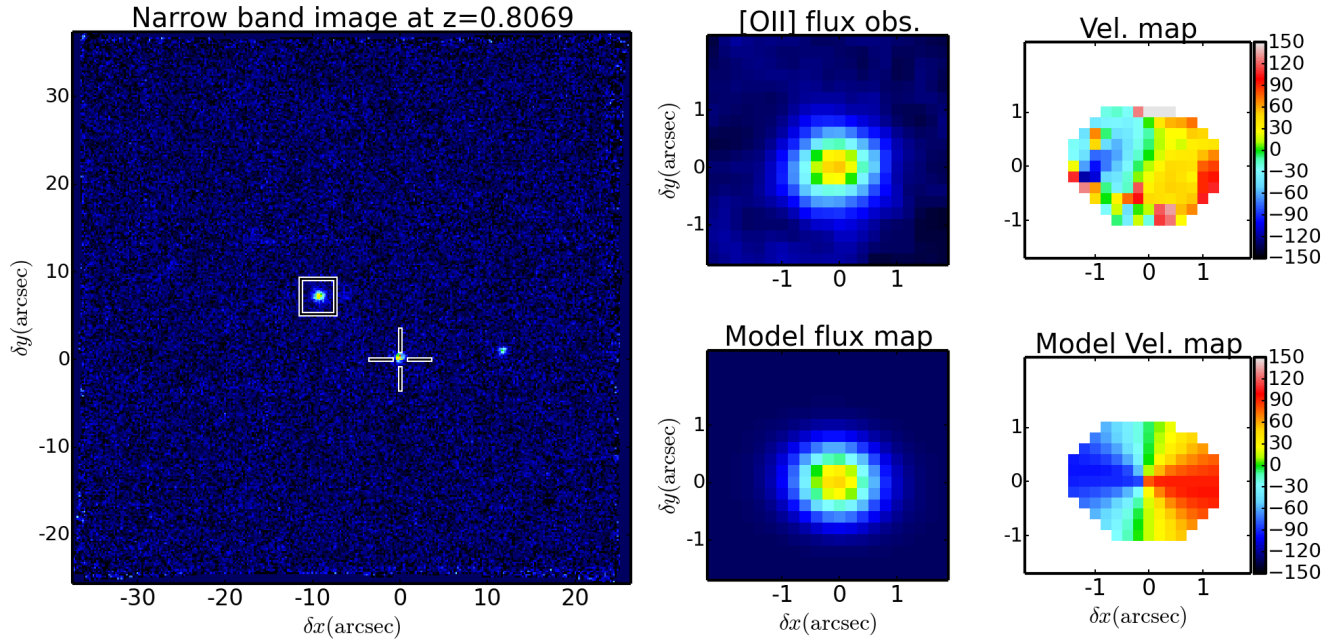


FIG. 3.— GalPaK and Camel results on galaxy J213748+0012G1. *Left:* Narrow band image for [O II] $\lambda 3727, 3729$ at redshift $z = 0.8069$. The quasar LOS is represented by the white cross and the galaxy is inside the white rectangle. The other spot on the right corresponds to continuum residuals from a star. *Right:* from left to right: [O II] doublet integrated flux and velocity maps. The top row corresponds to a 2×2 Gaussian smoothed flux map (the left panel) and Camel velocity map (top right). The bottom row represents the GalPaK^{3D} model flux (left) and PSF-deconvolved velocity maps (right). This galaxy has a maximum SNR/pixel of ≈ 11 .

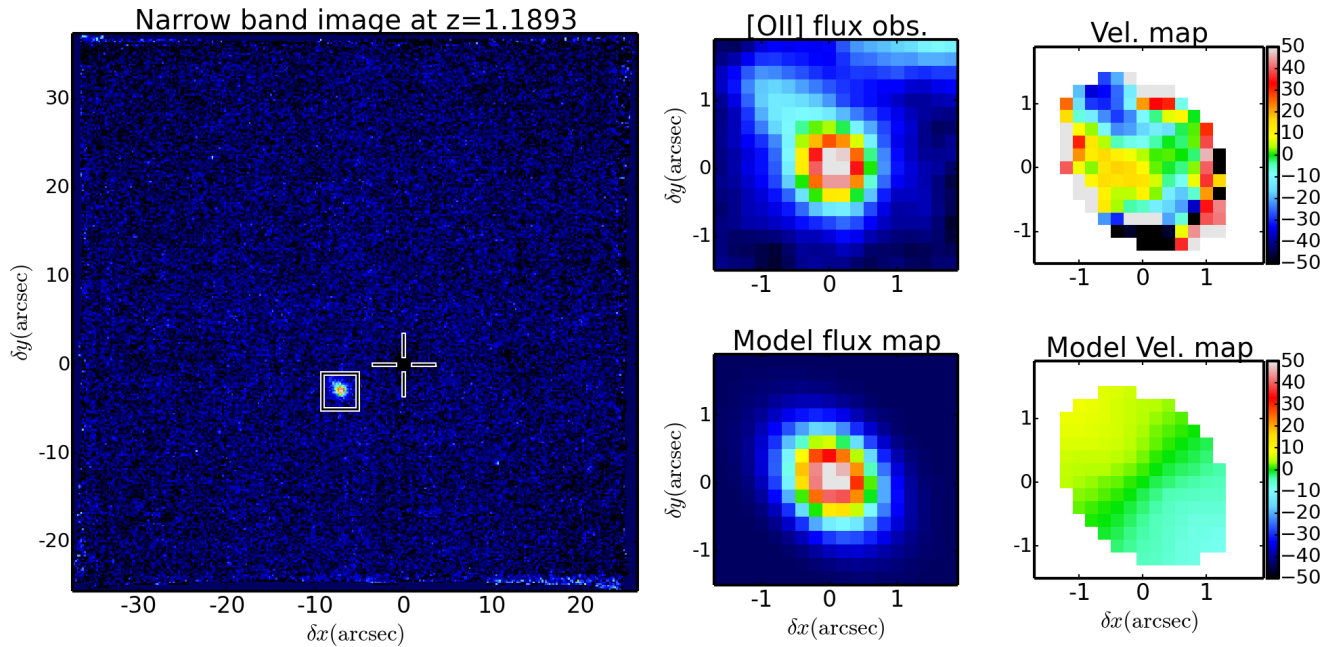


FIG. 4.— Same as Figure 3 but for J213748+0012G2 at redshift $z = 1.1893$. This galaxy has a maximum SNR/pixel of ≈ 11 . For this galaxy, we can see that the velocity maps do not agree with each other. Because one part of the galaxy is not reproduced by our model and clearly has a flux component (top middle panel), this galaxy seems to be a merger and therefore the azimuthal angle of this pair is not reliable.

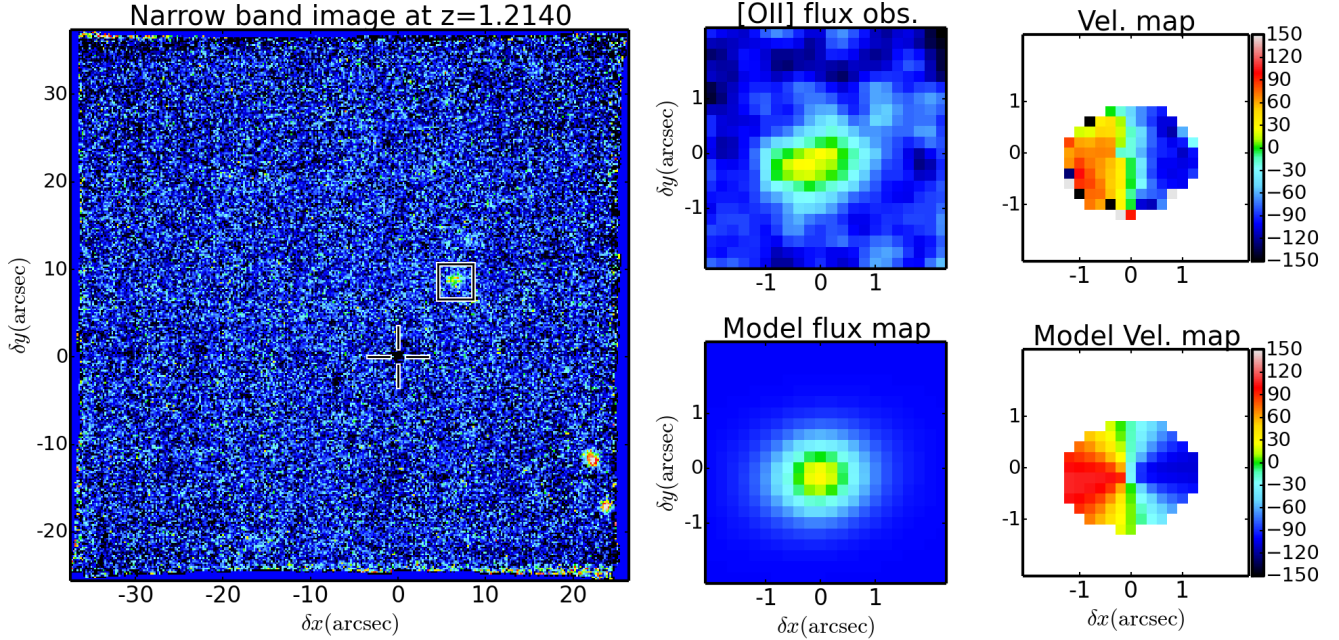


FIG. 5.— Same as Figure 3 but for J213748+0012G3 at redshift $z = 1.2140$. This galaxy has a maximum SNR/pixel of 4.5. The spots located bottom right in the narrow band image corresponds to other galaxies. These galaxy have very low probability to be the host of the Mg II absorption line in the quasar spectrum as they are located further away from the quasar LOS (212 kpc and 246 kpc).

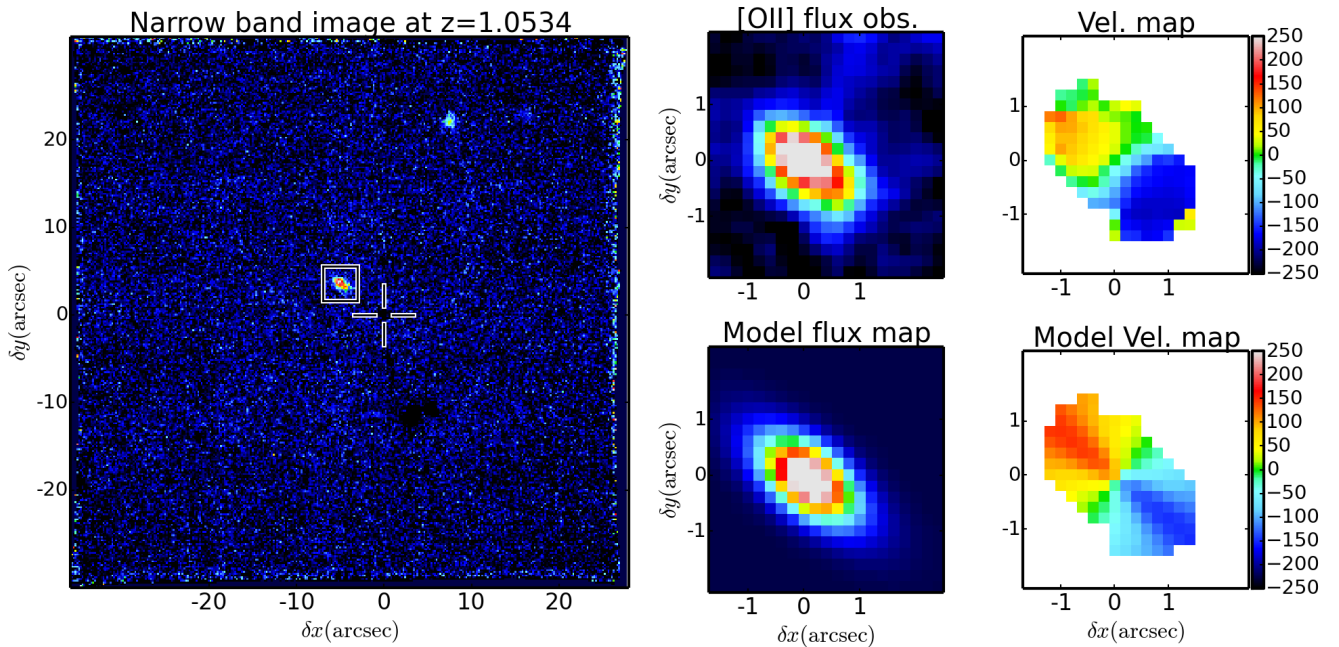


FIG. 6.— Same as Figure 3 but for J215200+0625G1 at redshift $z = 1.0534$. This galaxy has a maximum SNR/pixel of 9.3. The spot located top middle-right in the narrow band image corresponds to another galaxy. Like the one in Figure 5, this galaxy is less likely to be the host of the Mg II absorption line in the quasar spectrum as it is located further away from the quasar LOS (189 kpc).

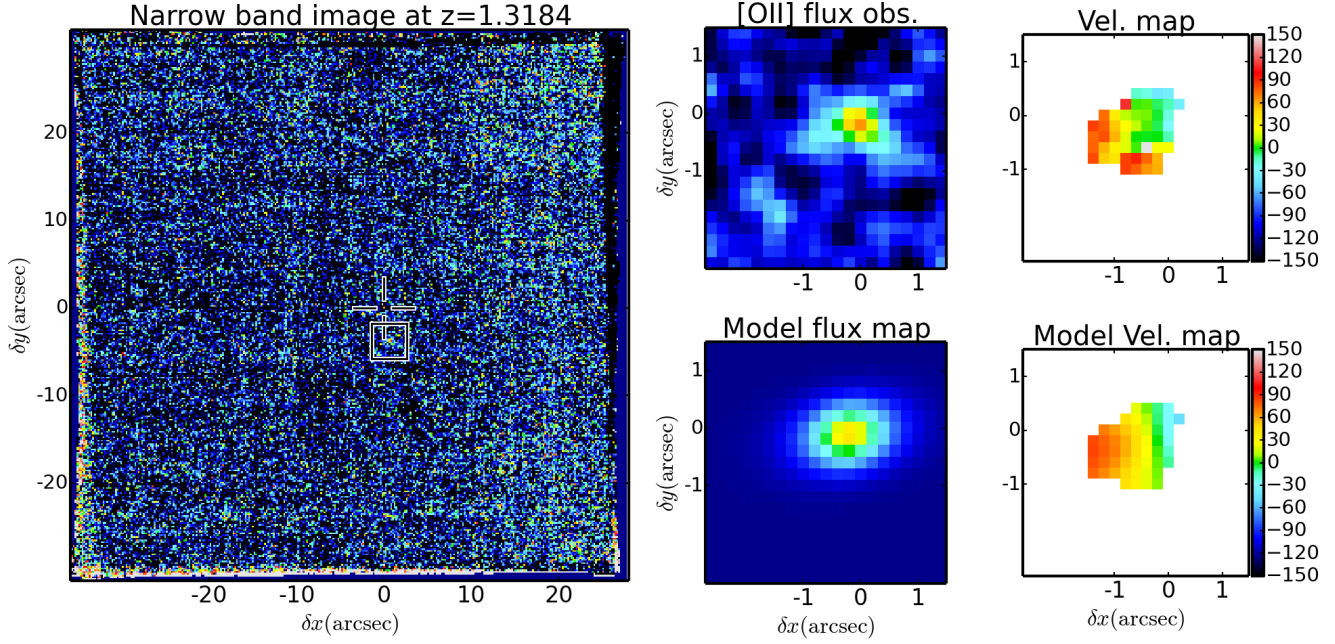


FIG. 7.— Same as Figure 3 but for J215200+0625G2 at redshift $z = 1.3184$. This galaxy has a maximum SNR/pixel of 4.2 and is thus difficult to see in the left image but can be seen in the smoothed [OII] flux image.

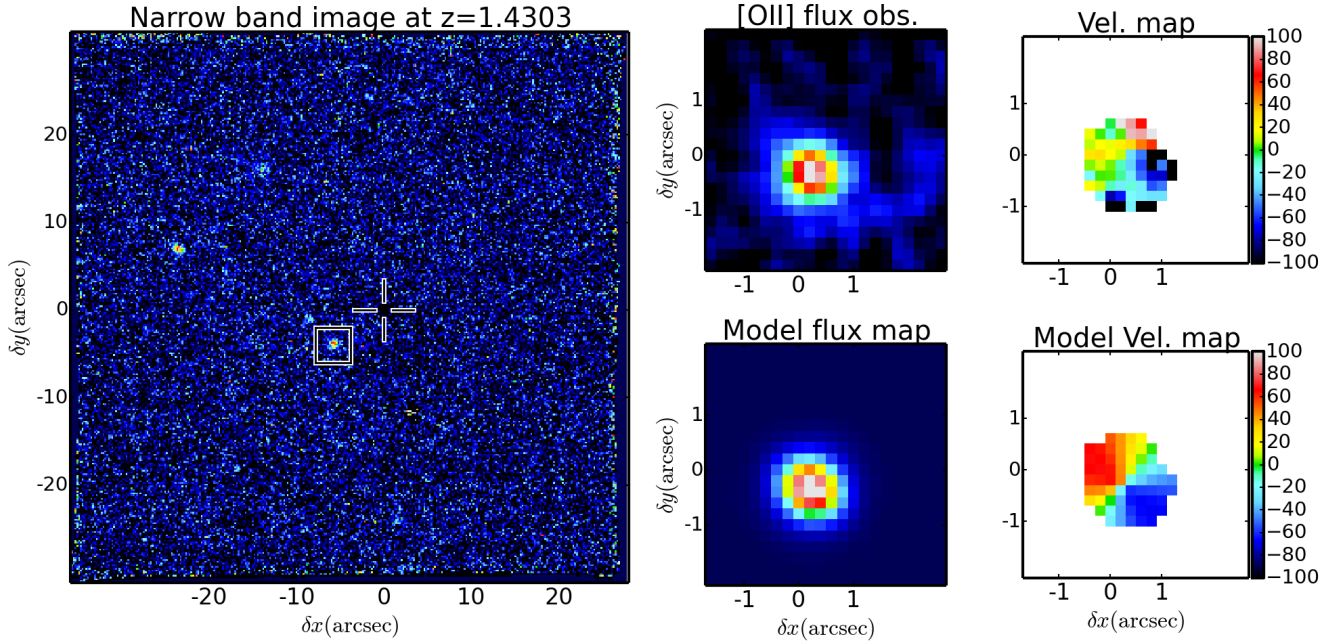


FIG. 8.— Same as Figure 3 but for J215200+0625G3 at redshift $z = 1.4303$. This galaxy has a maximum SNR/pixel of 10.5. Again, as in Figures 5 and 6, residual spots are galaxies further away from the quasar LOS and are thus less likely to be the host of the absorbing materials (78, 184 and 211 kpc). The 78 kpc away galaxy is close enough to be considered as an host galaxy but we choose to ignore it based on impact parameter argument.

TABLE 6
MORPHO-KINEMATICS RESULTS ON HOST GALAXIES.

Galaxy (1)	z_{abs} (2)	z_{gal} (3)	b (4)	SNR (5)	Size (6)	i (7)	V_{max} (8)	Flux (9)	α (10)	Class (11)
J213748+0012G1	0.8063	0.80690 ± 0.00001	88.1 ± 0.2	11	2.43 ± 0.06	49.6 ± 1.4	126.2 ± 5	8.67×10^{-17}	25 ± 1	Inflow
J213748+0012G2	1.1890	1.18925 ± 0.00001	63.7 ± 0.2	11	3.15 ± 0.08	55.6 ± 0.8	15.9 ± 8	1.47×10^{-16}	...	Merger
J213748+0012G3	1.2144	1.21397 ± 0.00003	87.2 ± 0.2	4.5	5.38 ± 0.33	40.4 ± 5.0	166.5 ± 18	4.18×10^{-17}	47 ± 2	Ambig.
J215200+0625G1	1.0534	1.05335 ± 0.00001	45.4 ± 0.2	9.3	5.52 ± 0.09	69.4 ± 0.7	161.4 ± 2	1.09×10^{-16}	4 ± 1	Inflow
J215200+0625G2	1.3190	1.31843 ± 0.00005	34.0 ± 0.2	4.2	3.06 ± 0.51	58.9 ± 10.8	130.6 ± 29	1.99×10^{-17}	88 ± 5	Wind
J215200+0625G3	1.4309	1.43033 ± 0.00004	62.5 ± 0.2	10.5	1.51 ± 0.12	13.3 ± 3.4	298.5 ± 39	5.05×10^{-17}	72 ± 20	Wind/Ambig.

(1) Quasar name; (2) Mg II absorption redshift; (3) Galaxy redshift; (4) Impact parameter (kpc); (5) SNR per pixel; (6) Galaxy half-light radius (kpc); (7) Galaxy inclination (degrees); (8) Galaxy maximum velocity (km s^{-1}); (9) Integrated [O II] flux of the galaxy ($\text{erg s}^{-1} \text{cm}^{-2}$); (10) Azimuthal angle (degrees); (11) Class (inflow-pair/wind-pair) based on α selection.

TABLE 7
UVES REST EQUIVALENT WIDTHS.

Galaxy (1)	$W_r^{\lambda 2796}$ (SDSS) (2)	$W_r^{\lambda 2796}$ (3)	$W_r^{\lambda 2802}$ (4)	$W_r^{\lambda 2852}$ (5)	$W_r^{\lambda 2586}$ (6)	$W_r^{\lambda 2600}$ (7)	$\log(N_{\text{H I}})$ (8)	Class (9)
J213748+0012G1	0.724 ± 0.09	0.789 ± 0.02	0.572 ± 0.02	0.145 ± 0.02	0.135 ± 0.02	0.309 ± 0.02	19.24	Inflow
J213748+0012G2	0.308 ± 0.06	0.294 ± 0.02	0.155 ± 0.02	0.039 ± 0.02	...	0.058 ± 0.02	18.61	Merger
J213748+0012G3	1.122 ± 0.06	1.132 ± 0.02	1.040 ± 0.02	0.223 ± 0.02	0.707 ± 0.02	0.947 ± 0.02	19.58	Ambig.
J215200+0625G1	0.522 ± 0.14	0.545 ± 0.02	0.460 ± 0.02	0.116 ± 0.02	0.175 ± 0.02	0.271 ± 0.02	19.01	Inflow
J215200+0625G2	1.347 ± 0.12	1.424 ± 0.02	1.065 ± 0.02	0.158 ± 0.02	0.322 ± 0.02	0.709 ± 0.02	19.71	Wind
J215200+0625G3	1.152 ± 0.11	1.157 ± 0.02	0.122 ± 0.02	0.242 ± 0.02	19.59	Wind/Ambig.

(1) Quasar name; (2) SDSS Mg II $\lambda 2796$ rest equivalent width (\AA); (3) UVES Mg II $\lambda 2796$ rest equivalent width (\AA); (4) UVES Mg II $\lambda 2802$ rest equivalent width (\AA); (5) UVES Mg I $\lambda 2852$ rest equivalent width (\AA); (6) UVES Fe II $\lambda 2586$ rest equivalent width (\AA); (7) UVES Fe II $\lambda 2600$ rest equivalent width (\AA); (8) Gas column density at the impact parameter (cm^{-2}); (9) Class (inflow-pair/wind-pair) based on α selection.

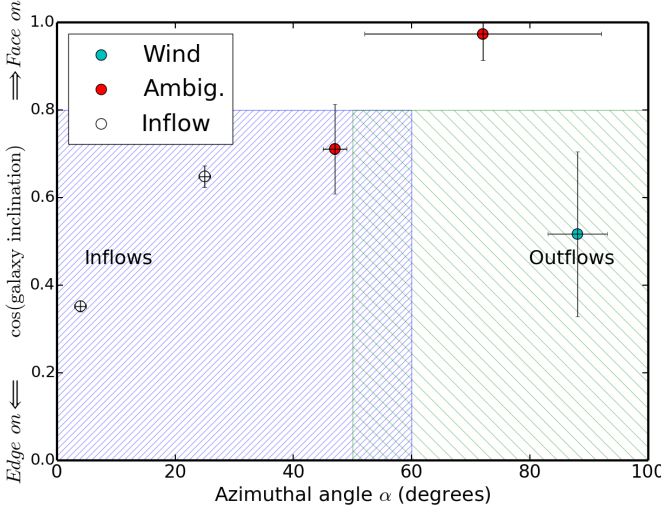


FIG. 9.— Galaxy inclinations as a function of azimuthal angle α for the 5 non-merger galaxies detected in the two fields J213748+0012 and J215200+0625. We note that only one galaxy is classified as a wind-pair. The dashed areas correspond to azimuthal angle ranges for which we classify pairs as inflow-pairs (blue and narrow dashes) or wind-pairs (green and wider dashes). These areas stop for face-on galaxies as uncertainty on position angles are too large and thus difficult to classify pairs.

described in § 4 but failed to reproduce this gap, even with stochastic effects. This lack of absorbing particles at these velocities shows that the outflowing cone must have a low density region inside it. Looking at the geometry of this galaxy-quasar system, the quasar line of sight is crossing the outflowing cone near its middle ($\alpha = 88^\circ$). In order to reproduce the absorption profile, we thus developed a partially empty cone model.

The principle is the same as the wind model described in § 4 except that we only fill the cone with particles from a certain opening angle θ_{in} to θ_{max} . This model should only work if the azimuthal angle α of a galaxy–quasar system is above $\sim 80^\circ$, so the quasar LOS is crossing this empty region and thus creating a gap of velocities in the simulated profile.

Figure 13 illustrates the resulting wind modeling for this galaxy. The first left column corresponds to the wind model representation. The top panel shows a [O II] integrated flux, continuum subtracted, image with the orange cross showing the quasar LOS position. The inclined circles represent the outflowing cone. The bottom panel represents a side view of the cone, the quasar LOS being represented by the dashed red line, the observer being on the left. This representation allows us to see if the outflowing material is ejected toward or away from us.

On the right column are represented the simulated profiles (top) and UVES spectrum around the absorption line Fe II $\lambda 2586$ (bottom). The red part of the simulated profile is the profile without instrumental noise and the apparent noise is due to stochastic effects from the Monte Carlo particle distribution. The red simulated absorption profile does not change much for the UVES data as compare to the noise-added one.

The bottom right panel corresponds to UVES data. Absorption lines are centered at the systemic velocity and are chosen to be unsaturated (since saturated ab-

sorption profiles could be broadened). The element Fe II $\lambda 2586$ corresponding to the absorption lines is shown in the bottom right panel.

To generate these simulated profiles, we adjust the outflow speed V_{out} and the cone opening angle θ_{max} while keeping the geometrical parameters of the galaxy fixed.

We note that we reproduce the equivalent width of the data and using the additional contribution model described above, we are able to reproduce the gap of velocities of this profile. With the context of our model, such a gap could not be reproduced by stochastic effects in generating lots of different simulated profiles. For this specific case, we derive an inner opening angle of the cone of $\theta_{\text{in}} \approx 7^\circ$.

The best values for reproducing the UVES Mg II $\lambda 2803$ absorption profile are an outflow velocity V_{out} of $150 \pm 10 \text{ km s}^{-1}$ and a cone opening angle θ_{max} of $20 \pm 5^\circ$.

Figure 11, middle column, shows the UVES Mg I $\lambda 2852$, Mg II $\lambda\lambda 2796, 2802$ and Fe II $\lambda\lambda 2586, 2600$ absorption lines for this galaxy-quasar pair. From this Figure, we can see that the Mg II $\lambda\lambda 2796, 2802$ absorption lines are saturated and thus the need to simulate the absorption from Fe II $\lambda 2586$ which is the only non-saturated absorption lines in the presented transitions.

4.2. Outflow rates

Having constrained the outflow velocity and cone opening angle for the wind-pair, we can now derive the ejected mass rate \dot{M}_{out} as well as the loading factor.

For our wind-pair, the equivalent width of the absorption lines only depends on θ_{max} and V_{out} (see § 4). After testing several opening angles and outflow velocities, we fitted the width of the absorption profile created by gas outflowing from the galaxy. The asymmetry of the profile depends on the system geometry. To constrain the ejected mass rate probed by the quasar LOS, we use relation 3 from Bouché et al. (2012) and Schroetter et al. (2015):

$$\dot{M}_{\text{out}} \approx \mu \cdot N_{\text{H}}(b) \cdot b \cdot V_{\text{out}} \cdot \frac{\pi}{2} \cdot \theta_{\text{max}} \quad (3)$$

$$\frac{\dot{M}_{\text{out}}}{0.5 M_{\odot} \text{ yr}^{-1}} \approx \frac{\mu}{1.5} \cdot \frac{N_{\text{H}}(b)}{10^{19} \text{ cm}^{-2}} \cdot \frac{b}{25 \text{ kpc}} \cdot \frac{V_{\text{out}}}{200 \text{ km s}^{-1}} \cdot \frac{\theta_{\text{max}}}{30^\circ}$$

μ being the mean atomic weight, b the impact parameter, θ_{max} the cone opening angle⁷, V_{out} the outflow velocity and $N_{\text{H}}(b)$ is the gas column density at the b distance.

The only parameter which is yet to be constrained is the gas column density $N_{\text{H}}(b)$. To do that, we use the empirical relation 4 from Ménard & Chelouche (2009) between the neutral gas column density and the Mg II $\lambda 2796$ REW $W_r^{\lambda 2796}$:

$$\log(N_{\text{HI}})(\text{cm}^{-2}) = \log[(3.06 \pm 0.55) \times 10^{19} \times (W_r^{\lambda 2796})^{1.7 \pm 0.26}] \quad (4)$$

To compute the errors, we assume a gaussian error distribution. As described in Schroetter et al. (2015), for regions with H I column density above $\log(N_{\text{HI}}) = 19.5$, the ionized gas contribution is negligible. Also argued by Jenkins (2009), if this column density is above this

⁷ θ_{max} is defined from the central axis, and the cone subtends an area Σ of $\pi \cdot \theta_{\text{max}}^2$.

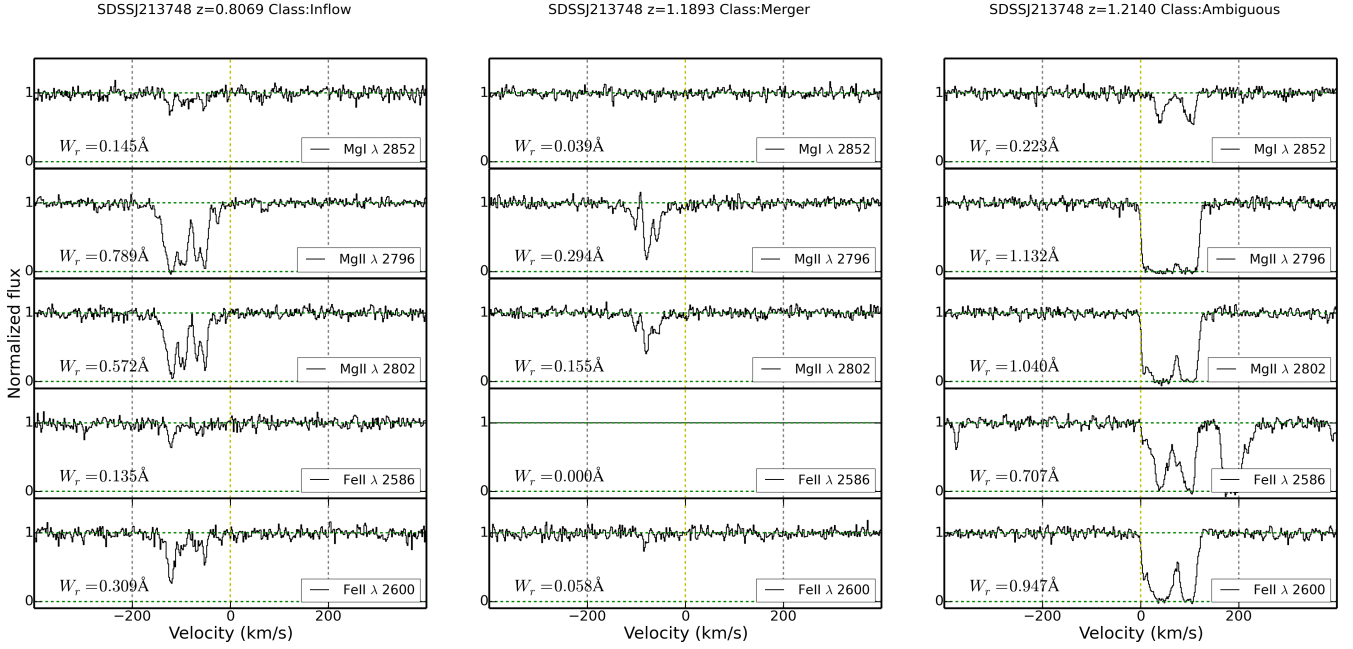


FIG. 10.— UVES Mg I λ 2852, Mg II $\lambda\lambda$ 2796, 2802 and Fe II $\lambda\lambda$ 2586, 2600 absorption lines centered at host galaxy systemic velocity for the SDSSJ213748+0012 quasar spectrum. The left panel corresponds to absorption lines from the SDSSJ213748+0012G1 host galaxy. The middle panel to the SDSSJ213748+0012G2 host galaxy, and right panel to SDSSJ213748+0012G3. Note that in the right column, the Fe II λ 2586 REW is calculated without the ≈ 200 km s $^{-1}$ absorption component.

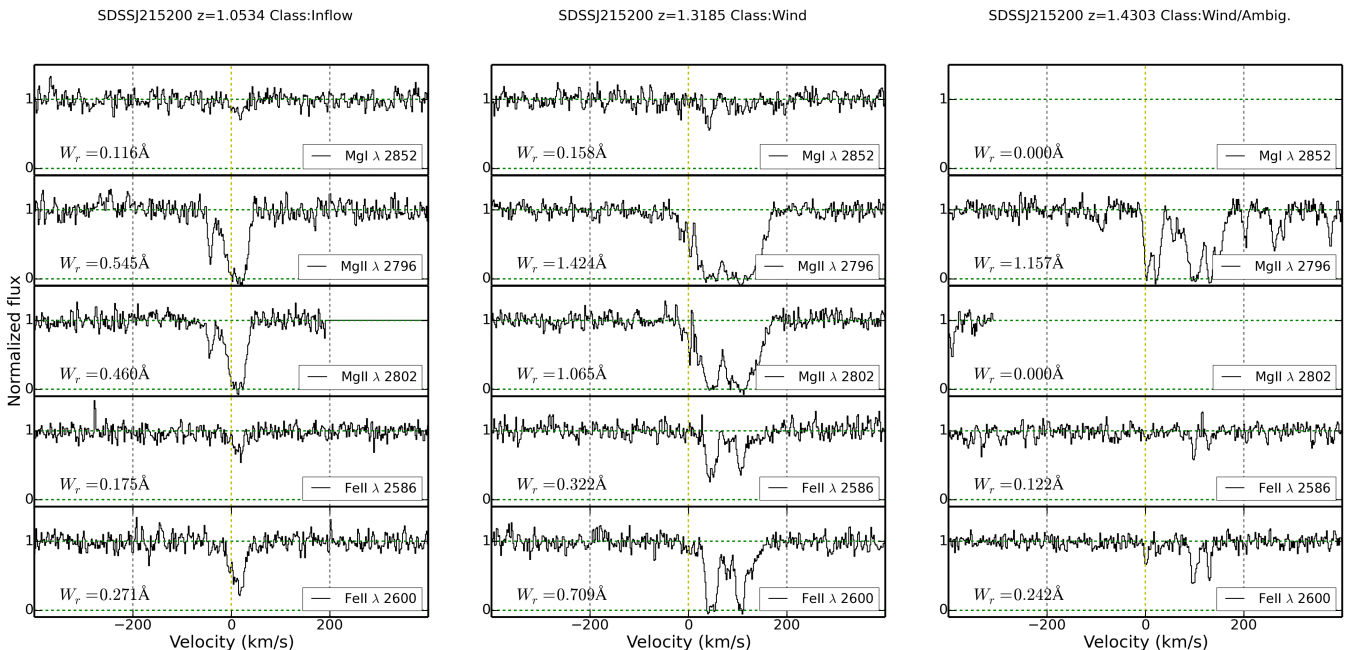


FIG. 11.— UVES Mg I λ 2852, Mg II $\lambda\lambda$ 2796, 2802 and Fe II $\lambda\lambda$ 2586, 2600 absorption lines centered at host galaxy systemic velocity for the SDSSJ215200+0625 quasar spectrum. The left panel corresponds to absorption lines from the SDSSJ215200+0625G1 host galaxy. The middle panel to the SDSSJ215200+0625G2 host galaxy, and right panel to SDSSJ215200+0625G3.

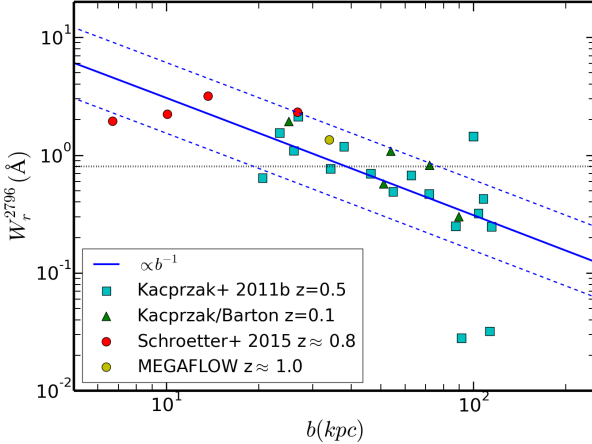


FIG. 12.— $W_r^{\lambda 2796}$ as a function of impact parameter b for galaxy-quasar pairs classified as wind-pairs. The dashed blue lines show the 0.3 dex scatter. The horizontal dotted black line represents the $W_r^{\lambda 2796}=0.8$ Å selection limit.

limit, one can use the correlation between Mg II equivalent width and N_{HI} as a proxy for the N_{H} gas column density. For the wind-pair J215200+0625G2, we have a gas column density of $\log(N_{\text{HI}}) \approx 19.7 \pm 0.07$.

Another aspect of outflow properties is whether the outflowing gas is able to escape from the galaxy gravitational well. To determine this, we derive the escape velocity V_{esc} for the J215200+0625G2 galaxy. The escape velocity for an isothermal sphere is defined by Eq. 5 (Veilleux et al. 2005).

$$V_{\text{esc}} = V_{\text{max}} \cdot \sqrt{2 \left[1 + \ln \left(\frac{R_{\text{vir}}}{r} \right) \right]} \quad (5)$$

V_{max} being the maximum rotation velocity of the galaxy and R_{vir} its virial radius. The virial radius of the galaxies can be defined as $R_{\text{vir}} \approx V_{\text{max}}/10H(z)$ where $H(z)$ is the Hubble parameter at redshift z . In Table 8, we compare the outflow velocity with the escape velocity for the wind-pair. The outflowing material is not able to reach the escape velocity and will thus likely to fall back onto the galaxy, assuming we are tracing the gas going out of the galaxy. One can ask whether we are already tracing the gas falling back onto the galaxy. If this is the case, we should see another opposite component (with respect to the systemic velocity) in the absorption profile corresponding to the outflowing gas. Hence, the outflowing gas collimated in a cone should have a larger column density than the falling-back gas if we assume a “fountain” behavior of outflows.

Table 8 also lists the estimated outflow rate. The errors on the ejected mass rate M_{out} are dominated by the ones on the gas column density N_{HI} and the SFR.

From the outflow rate, we compute the mass loading factor η by comparing it to the SFR. For our SDSSJ215200+0625G2 pair, we used the partially empty cone model to reproduce the absorption profile. To be consistent with the other cases, we give two solutions for this galaxy–quasar pair: one with the filled cone and one with the inner cone subtracted.

Figure 14 shows the loading factor η as a function of halo mass and maximum rotational velocity V_{max} for this work and previous similar studies (Bouché et al. 2012;

Kacprzak et al. 2014; Schroetter et al. 2015). The derived loading factor for galaxy SDSSJ215200+0625G2 follows the same trend as the others. The green arrow shows the loading factor for the subtracted mass from the low-density inner cone.

MUSE allows us to probe galaxies with an impact parameter larger than before with an IFU. But, in Figure 14, we caution the reader that loading factor for galaxies with impact parameters larger than 60 kpc are less reliable because of the time needed for the gas to travel from the galaxy to the quasar LOS. A major limitation for the comparison between data and models in Figure 14, is that η in simulations are usually measured on a scale of a few kpc away from the galaxy, which is one order of magnitude lower than most of the observations (tens of kpc).

5. DISCUSSION AND CONCLUSIONS

We present results on 2 GTO VLT/MUSE fields in which we searched for galaxy-quasar pairs. These fields were selected from the SDSS database where we searched for multiple Mg II absorbers, with $z \approx 0.8 - 1.4$ and $W_r^{\lambda 2796} > 0.8$ Å, in the quasar spectra. Out of 8 Mg II absorptions in the quasar spectra of these two fields, we detect 6 redshift-corresponding SFGs. For these 2 fields (J213748+1112 and J215200+0625) we also have high resolution spectra of the quasars from the VLT/UVES instrument. In each of these two fields, we detected more than 40 emitters in the $1' \times 1'$ MUSE field of view (see the Appendix). We focused on galaxies at MgII absorptions redshifts in the quasar spectra and for which the associated quasar LOS is aligned with their minor axis ($\alpha > 45^\circ$) and is thus likely to probe outflowing materials (wind–pairs). Among the 6 detected SFGs, one is likely to be a wind-pair due to its orientation with respect to its relative quasar.

In summary, thanks to our new GTO VLT/MUSE and VLT/UVES data, MUSE allows us to detect galaxies far away from their associated quasar (~ 100 kpc) as compare to previous similar works (i.e. Bouché et al. 2012; Kacprzak et al. 2014; Schroetter et al. 2015). For the wind-pair SDSSJ215200+0625G2, we found that the outflow velocity V_{out} is ≈ 150 km s $^{-1}$. The outflowing gas is likely to stay inside the gravitational well of the galaxy and the loading factor is $\eta \approx 0.7$. We showed a gap in velocities in the absorption profile which led to a low-density inner cone modeling. At this point, we have outflowing constraints for one galaxy but we showed that MUSE is able to provide very good data and will play a fundamental role in this field.

MUSE allowed us to probe multiple galactic wind cases at the same time and enhance the number of cases with only two quasar fields. We also have a case of low-density inner cone which opens discussions on geometrical properties of outflowing materials. The MEGAFLOW sample is currently growing and successful in detecting galaxies in each quasar field. Future work will be done with a lot more observation with MUSE+UVES, and in a short time, the MEGAFLOW sample should be large enough to produce statistical results on outflow properties.

Acknowledgments. NB acknowledges support from a Career Integration Grant (CIG) (PCIG11-GA-2012-

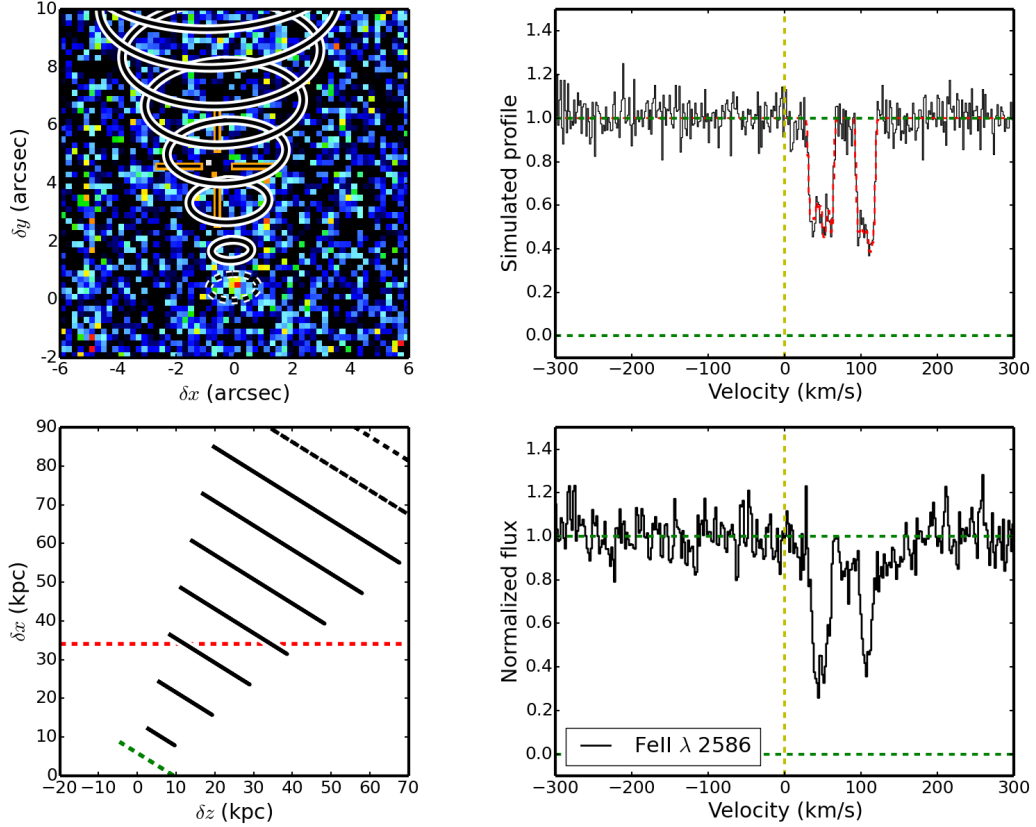


FIG. 13.— Representation of the cone model and quasar spectrum associated with the J215200+0625G2 galaxy ($z = 1.31845$). *Top left*: the cone model seen in the sky plane (xy). This is a narrow band image centered around the galaxy [O II] emission lines with the continuum subtracted. The dashed circle represents the inclined galaxy disk and the black and white inclined circles illustrate the gas outflow cone. The orange cross represents the position of the quasar LOS. *Bottom left*: a side view of the cone where the z-axis corresponds to the quasar LOS direction with the observer to the left. *Right*: Normalized flux for the Fe II ($\lambda 2586$) absorption line observed with UVES (bottom) and the reconstructed profile (top). Note that this model does not reproduce the depth of the absorption line. In UVES simulated absorption profile, the red line corresponds to the simulated profile without any instrumental noise. This wind model uses a very low-density inner cone as described in § 4.1. This outflow has a V_{out} of $150 \pm 10 \text{ km s}^{-1}$, a cone opening angle θ_{max} of $20 \pm 5^\circ$ and an inner opening angle θ_{in} of $7 \pm 2^\circ$.

TABLE 8
RESULTS FOR THE GALAXY J215200+0625G2.

Galaxy	b (kpc)	$\log(N_{\text{H}}(b))$	V_{max}	V_{out}	θ_{max}	SFR	\dot{M}_{out}	$\frac{V_{\text{out}}}{V_{\text{esc}}}$	η
(1)	(2)	(3)	(4)	(5)	(6)	(7)	(8)	(9)	(10)
J215200+0625G2	34.0	19.7 ± 0.07	140.8 ± 51	150 ± 10	20 ± 5.0	4.6 ± 0.4	$1.7^{+1.1}_{-0.8}$	0.52	0.75
							$1.1^{+0.9}_{-0.6}$		0.49

(1) Galaxy name; (2) Impact parameter (kpc); (3) Gas column density at the impact parameter (cm^{-2}); (4) Maximum rotational velocity of the galaxy (km s^{-1}); (5) Wind velocity (km s^{-1}); (6) Cone opening angle (degrees) (7) Star Formation Rate ($\text{M}_{\odot} \text{ yr}^{-1}$); (8) Ejected mass rate for one cone ($\text{M}_{\odot} \text{ yr}^{-1}$); (9) Ejection velocity divided by escape velocity; (10) Mass loading factor: ejected mass rate divided by star formation rate (for both cones).

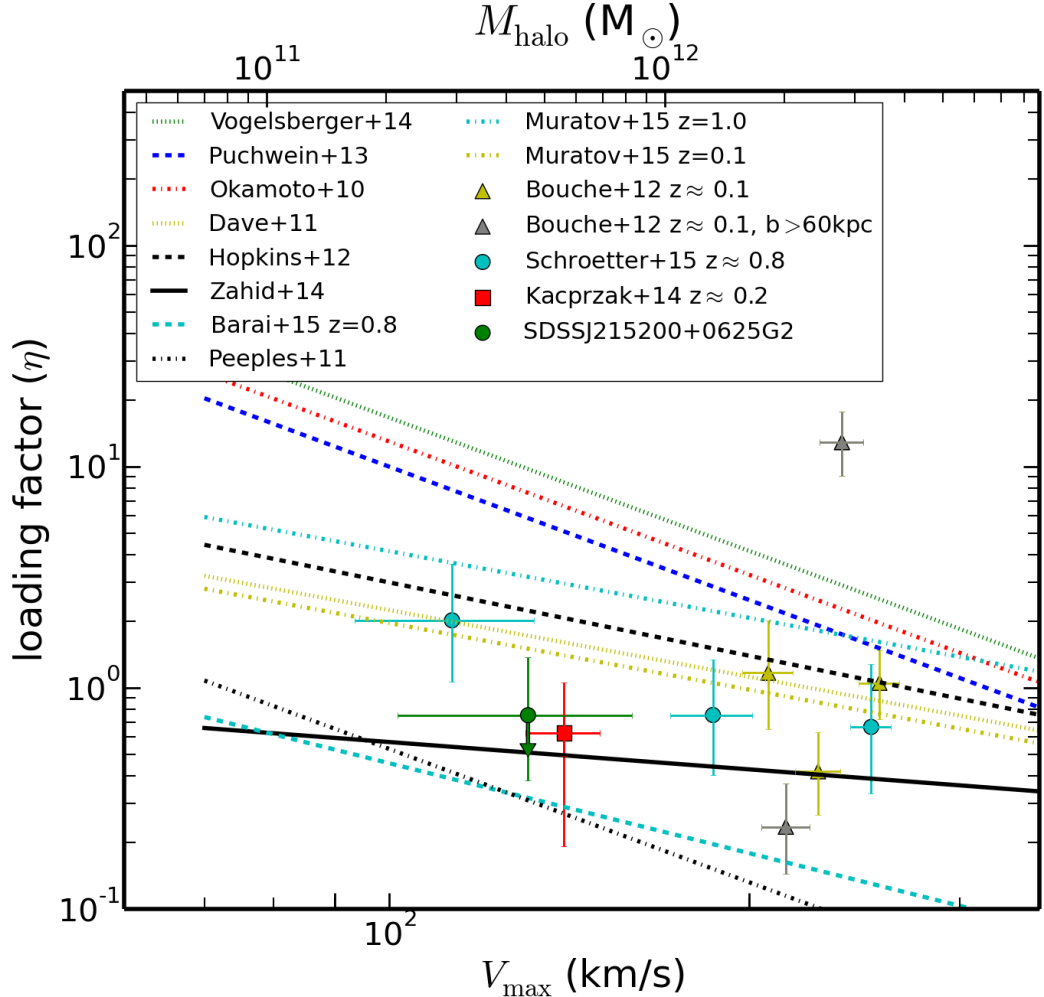


FIG. 14.— Comparison of mass loading factors assumed by theoretical/empirical models (curves) with values derived from observations (dots and triangles) as a function of the maximum rotational velocity. The result from this work is represented by the green circle. The green arrow represents the loading factor of the SDSSJ215200+0625G2 galaxy with the subtracted mass from the inner cone model. The cyan circles show the results for galaxies at $z \approx 0.8$ from Schroetter et al. (2015). The red square shows the mass loading factor for a $z \approx 0.2$ galaxy (Kacprzak et al. 2014). The triangles show the results for $z \approx 0.2$ galaxies from Bouché et al. (2012). The gray triangles show the galaxies with quasars located at $>60\text{kpc}$ where the mass loading factor is less reliable due to the large travel time needed for the outflow to cross the quasar LOS (several 100 Myr) compared to the short time scale of the H α derived SFR ($\sim 10\text{Myr}$). The upper halo mass axis is scaled on V_{max} at redshift 0.8 from Mo & White (2002).

321702) within the 7th European Community Framework Program. This work has been carried out thanks to the support of the ANR FOGHAR (ANR-13-BS05-0010-02), the OCEVU Labex (ANR-11-LABX-0060) and the A*MIDEX project (ANR-11-IDEX-0001-02) funded by the “Investissements d’Avenir” French government program managed by the ANR. This work received financial support from the European Research Council under the European Union’s Seventh Framework Programme (FP7/2007-2013) / ERC Grant agreement 278594-GasAroundGalaxies.

REFERENCES

Aguirre, A., Hernquist, L., Schaye, J., et al. 2001, *ApJ*, 561, 521

Alam, S., Albareti, F. D., Allende Prieto, C., et al. 2015, ArXiv e-prints, arXiv:1501.00963

Bacon, R., Bauer, S., Boehm, P., et al. 2006, in Society of Photo-Optical Instrumentation Engineers (SPIE) Conference Series, Vol. 6269, Society of Photo-Optical Instrumentation Engineers (SPIE) Conference Series, 0

Bacon, R., Bauer, S., Brau-Nogu  , S., et al. 2009, *Astrophysics and Space Science Proceedings*, 9, 331

Barai, P., Monaco, P., Murante, G., Ragagnin, A., & Viel, M. 2015, *MNRAS*, 447, 266

Behroozi, P. S., Wechsler, R. H., & Conroy, C. 2013, *ApJ*, 770, 57

Booth, C. M., Agertz, O., Kravtsov, A. V., & Gnedin, N. Y. 2013, *ApJ*, 777, L16

Bordoloi, R., Lilly, S. J., Kacprzak, G. G., & Churchill, C. W. 2014, *ApJ*, 784, 108

Bordoloi, R., Lilly, S. J., Knobel, C., et al. 2011, *ApJ*, 743, 10

Bouch  , N., Carfantan, H., Schroetter, I., Michel-Dansac, L., & Contini, T. 2015, GalPaK 3D: Galaxy parameters and kinematics extraction from 3D data, *Astrophysics Source Code Library*, ascl:1501.014

Bouch  , N., Hohensee, W., Vargas, R., et al. 2012, *MNRAS*, 426, 801

Bouch  , N., Finley, H., Schroetter, I., et al. 2016, ArXiv e-prints, arXiv:1601.07567

Chabrier, G. 2003, *PASP*, 115, 763

Charlot, S., Kauffmann, G., Longhetti, M., et al. 2002, *MNRAS*, 330, 876

Chisholm, J., Tremonti, C. A., Leitherer, C., Chen, Y., & Wofford, A. 2016, ArXiv e-prints, arXiv:1601.05090

Chisholm, J., Tremonti, C. A., Leitherer, C., et al. 2015, *ApJ*, 811, 149

Dekel, A., & Silk, J. 1986, *ApJ*, 303, 39

Dekker, H., D'Odorico, S., Kaufer, A., Delabre, B., & Kotzlowski, H. 2000, in Society of Photo-Optical Instrumentation Engineers (SPIE) Conference Series, Vol. 4008, Optical and IR Telescope Instrumentation and Detectors, ed. M. Iye & A. F. Moorwood, 534–545

Epinat, B., Tasca, L., Amram, P., et al. 2012, *A&A*, 539, A92

Guo, Q., White, S., Li, C., & Boylan-Kolchin, M. 2010, *MNRAS*, 404, 1111

Heckman, T. M., Alexandroff, R. M., Borthakur, S., Overzier, R., & Leitherer, C. 2015, *ApJ*, 809, 147

Heckman, T. M., Armus, L., & Miley, G. K. 1990, *ApJS*, 74, 833

Heckman, T. M., Lehnert, M. D., Strickland, D. K., & Armus, L. 2000, *ApJS*, 129, 493

Hopkins, P. F. 2015, *MNRAS*, 450, 53

Hopkins, P. F., Kere  , D., O  orbe, J., et al. 2014, *MNRAS*, 445, 581

Jenkins, E. B. 2009, *ApJ*, 700, 1299

Kacprzak, G. G., Churchill, C. W., Barton, E. J., & Cooke, J. 2011a, *ApJ*, 733, 105

Kacprzak, G. G., Churchill, C. W., Evans, J. L., Murphy, M. T., & Steidel, C. C. 2011b, *MNRAS*, 416, 3118

Kacprzak, G. G., Martin, C. L., Bouch  , N., et al. 2014, *ApJ*, 792, L12

Kennicutt, Jr., R. C. 1998, *ApJ*, 498, 541

Kewley, L. J., Geller, M. J., & Jansen, R. A. 2004, *AJ*, 127, 2002

Lanzetta, K. M., & Bowen, D. 1990, *ApJ*, 357, 321

Lehnert, M. D., & Heckman, T. M. 1996, *ApJ*, 472, 546

Martin, C. L. 1998, *ApJ*, 506, 222

—. 1999, *ApJ*, 513, 156

—. 2005, *ApJ*, 621, 227

Martin, C. L., Kobulnicky, H. A., & Heckman, T. M. 2002, *ApJ*, 574, 663

Martin, C. L., Shapley, A. E., Coil, A. L., et al. 2012, *ApJ*, 760, 127

—. 2013, *ApJ*, 770, 41

M  nard, B., & Chelouche, D. 2009, *MNRAS*, 393, 808

Mo, H. J., & White, S. D. M. 2002, *MNRAS*, 336, 112

Moster, B. P., Naab, T., & White, S. D. M. 2013, *MNRAS*, 428, 3121

Moster, B. P., Somerville, R. S., Maulbetsch, C., et al. 2010, *ApJ*, 710, 903

Muratov, A. L., Keres, D., Faucher-Giguere, C.-A., et al. 2015, ArXiv e-prints, arXiv:1501.03155

Murray, N., Quataert, E., & Thompson, T. A. 2005, *ApJ*, 618, 569

Muzahid, S., Kacprzak, G. G., Churchill, C. W., et al. 2015, *ApJ*, 811, 132

Oppenheimer, B. D., & Dav  , R. 2006, *MNRAS*, 373, 1265

Oppenheimer, B. D., Dav  , R., Kere  , D., et al. 2010, *MNRAS*, 406, 2325

Papastergis, E., Cattaneo, A., Huang, S., Giovanelli, R., & Haynes, M. P. 2012, *ApJ*, 759, 138

Pettini, M., Rix, S. A., Steidel, C. C., et al. 2002, *ApJ*, 569, 742

Ross, N. P., Myers, A. D., Sheldon, E. S., et al. 2012, *ApJS*, 199, 3

Rubin, K. H. R., Weiner, B. J., Koo, D. C., et al. 2010, *ApJ*, 719, 1503

Rupke, D. S., Veilleux, S., & Sanders, D. B. 2005, *ApJS*, 160, 115

Salem, M., & Bryan, G. L. 2014, *MNRAS*, 437, 3312

Salpeter, E. E. 1955, *ApJ*, 121, 161

Schaye, J., Dalla Vecchia, C., Booth, C. M., et al. 2010, *MNRAS*, 402, 1536

Schaye, J., Crain, R. A., Bower, R. G., et al. 2015, *MNRAS*, 446, 521

Schroetter, I., Bouch  , N., P  roux, C., et al. 2015, *ApJ*, 804, 83

Soto, K. T., Lilly, S. J., Bacon, R., Richard, J., & Conseil, S. 2016a, *MNRAS*, submitted (astro-ph/1602.08037), arXiv:1602.08037

—. 2016b, ZAP: Zurich Atmosphere Purge, *Astrophysics Source Code Library*, ascl:1602.003

Springel, V., & Hernquist, L. 2003, *MNRAS*, 339, 289

Springel, V., White, S. D. M., Jenkins, A., et al. 2005, *Nature*, 435, 629

Steidel, C. C. 1995, in *QSO Absorption Lines*, ed. G. Meylan, 139

Torrey, P., Vogelsberger, M., Genel, S., et al. 2014, *MNRAS*, 438, 1985

Veilleux, S., Cecil, G., & Bland-Hawthorn, J. 2005, *ARA&A*, 43, 769

Vogelsberger, M., Genel, S., Springel, V., et al. 2014, *Nature*, 509, 177

Weilbacher, P. M., Streicher, O., Urrutia, T., et al. 2014, in *Astronomical Society of the Pacific Conference Series*, Vol. 485, *Astronomical Data Analysis Software and Systems XXIII*, ed. N. Manset & P. Forshay, 451

Wood, C. M., Tremonti, C. A., Calzetti, D., et al. 2015, *MNRAS*, 452, 2712

Zahid, H. J., Torrey, P., Vogelsberger, M., et al. 2014, *Ap&SS*, 349, 873

Zhu, G., & M  nard, B. 2013, *ApJ*, 770, 130

TABLE 9
MUSE SOURCES IN THE SDSSJ213748+0012 FIELD WITH REDSHIFTS. WITHIN THESE 42 EMITTERS, 36 HAVE IDENTIFIED EMISSION LINES.

ID	R.A.	Dec.	redshift	lines
obj001	21:37:48.303	+00:12:21.69	0.132	OIII, H $_{\beta}$, H $_{\alpha}$, NII
obj002	21:37:48.757	+00:12:19.29	0.156	OIII, H $_{\beta}$, H $_{\alpha}$, NII
obj003	21:37:50.157	+00:12:52.89	0.315	H $_{\beta}$, OIII
obj004	21:37:48.370	+00:12:23.89	0.325	OII, OIII, H $_{\beta}$, H $_{\alpha}$, NII
obj005	21:37:48.370	+00:12:24.09	0.325	OII, OIII, H $_{\beta}$, H $_{\alpha}$
obj006	21:37:48.930	+00:12:38.69	0.409	OII, OIII, H $_{\alpha}$, NII
obj007	21:37:49.223	+00:12:20.09	0.410	OII, OIII, H $_{\beta}$
obj008	21:37:49.810	+00:12:15.69	0.442	OII
obj009	21:37:48.477	+00:12:30.09	0.543	OII, OIII, H $_{\beta}$
obj010	21:37:48.450	+00:12:29.49	0.543	OII, OIII, H $_{\beta}$
obj011	21:37:50.450	+00:12:02.89	0.580	OIII, H $_{\beta}$
obj012	21:37:48.983	+00:12:55.09	0.616	OII, OIII, H $_{\beta}$
obj013	21:37:49.343	+00:12:52.09	0.684	OII, OIII, H $_{\beta}$
obj014	21:37:47.743	+00:12:46.69	0.711	OII
obj015	21:37:49.530	+00:12:14.69	0.766	OII
obj016	21:37:48.317	+00:12:15.69	0.767	OII
obj017	21:37:49.463	+00:12:16.49	0.767	OII, OIII
obj018	21:37:49.023	+00:12:27.29	0.806	OII, OIII, H $_{\beta}$
obj019	21:37:48.823	+00:12:27.49	0.806	OII, OIII
obj020	21:37:50.157	+00:12:30.89	0.806	OII, OIII
obj021	21:37:49.490	+00:12:33.69	...	8281.3
obj022	21:37:50.103	+00:12:53.29	...	6823.
obj023	21:37:49.117	+00:12:11.89	...	6897.
obj024	21:37:47.663	+00:12:12.69	0.900	OII
obj025	21:37:48.930	+00:12:09.49	0.902	OII?
obj026	21:37:48.517	+00:12:05.69	...	7079.69
obj027	21:37:48.063	+00:12:33.69	...	7376.81
obj028	21:37:48.437	+00:12:46.29	1.010	OII
obj029	21:37:48.837	+00:12:42.69	1.010	OII
obj030	21:37:48.970	+00:12:09.49	1.045	OII
obj031	21:37:49.970	+00:12:09.09	1.044	OII
obj032	21:37:49.970	+00:12:15.29	1.122	OII
obj033	21:37:48.903	+00:12:17.69	1.188	OII
obj034	21:37:46.837	+00:12:02.89	1.212	OII
obj035	21:37:47.970	+00:12:29.09	1.213	OII
obj036	21:37:46.943	+00:12:08.89	1.214	OII
obj037	21:37:47.850	+00:12:33.49	1.214	OII
obj038	21:37:50.410	+00:12:20.09	1.257	OII
obj039	21:37:48.370	+00:12:04.69	1.300	OII
obj040	21:37:47.717	+00:12:46.89	...	8569.12
obj041	21:37:48.730	+00:12:15.29	5.941	8434.53 Ly α ?
obj042	21:37:48.823	+00:12:27.49	6.442	9043.03 Ly α ?

APPENDIX

MUSE FIELDS EMITTERS DETECTION

For completeness we looked for these emitters by visual inspection and found 42 galaxies with emission lines in each of these two fields (see Table 9 for SDSSJ213748+0012 and Table 10 for SDSSJ215200+0625).

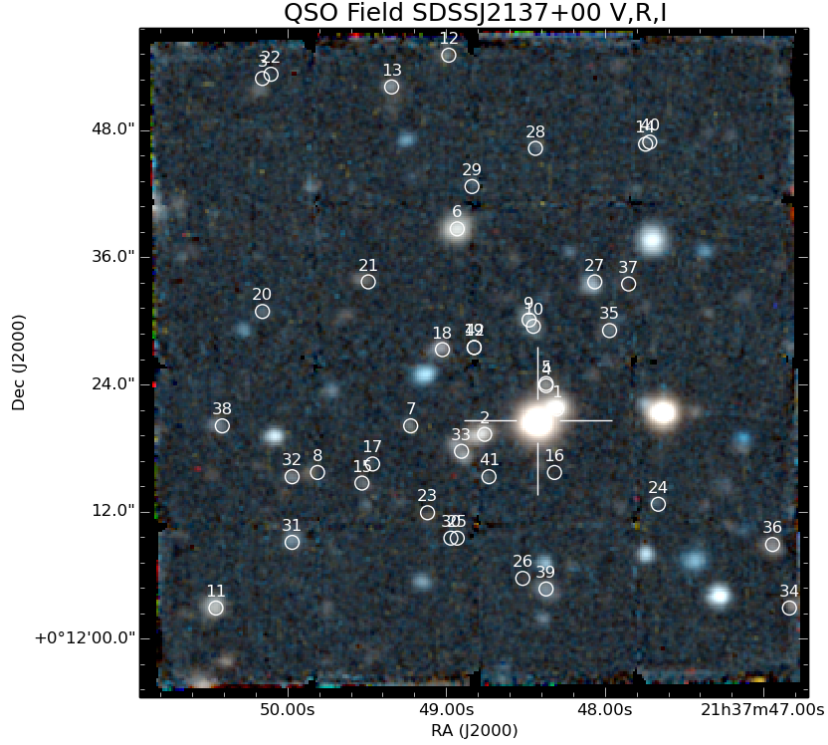


FIG. A.1.— RGB image of the J213748+0012 field with identifications of emission detected galaxies. The white cross points the quasar location. Circles represent emission detected galaxies corresponding to Table 9. Not all the galaxy-like spots are circled on the image. These spots are either stars or galaxies with a continuum but without obvious emission line.

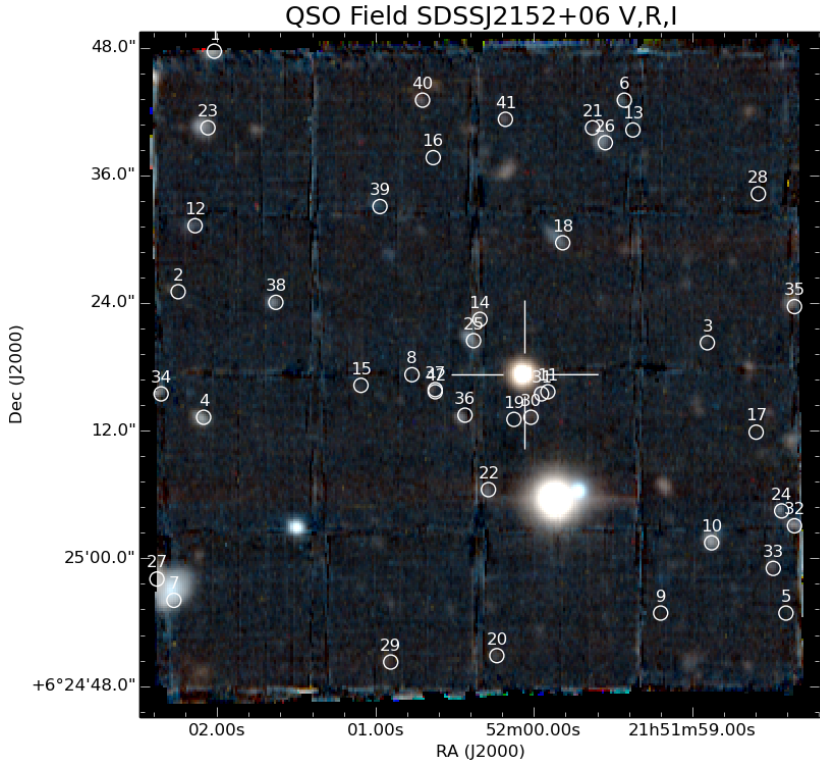


FIG. A.2.— Same as Figure A.1 but for the J215200+0625 quasar field. Again, the white cross shows the quasar location and galaxies with emission lines are circled and listed in Table 10.

TABLE 10

MUSE SOURCES IN THE SDSSJ215200+0625 FIELD WITH REDSHIFTS. WE FOUND 40 GALAXIES OUT OF 42 HAVING IDENTIFIED EMISSION LINES

ID	R.A.	Dec.	redshift	lines
obj001	21:52:02.018	+06:25:47.66	0.433	OII, OIII, H $_{\beta}$
obj002	21:52:02.246	+06:25:25.06	0.439	OII
obj003	21:51:58.905	+06:25:20.26	0.452	OII, OIII, H $_{\beta}$
obj004	21:52:02.085	+06:25:13.26	0.489	OII, OIII, H $_{\beta}$
obj005	21:51:58.409	+06:24:54.86	0.517	OII
obj006	21:51:59.429	+06:25:43.06	0.554	OII, OIII
obj007	21:52:02.273	+06:24:56.06	0.597	OII, OIII, H $_{\beta}$
obj008	21:52:00.770	+06:25:17.26	3.931?	5992.37 Ly α ?
obj009	21:51:59.200	+06:24:54.86	4.196?	6314.05 Ly α ?
obj010	21:51:58.878	+06:25:01.46	0.742	OII, OIII, H $_{\beta}$
obj011	21:51:59.912	+06:25:15.66	0.748	OII, H $_{\beta}$
obj012	21:52:02.139	+06:25:31.26	0.770	OII, OIII, H $_{\beta}$
obj013	21:51:59.375	+06:25:40.26	0.786	OII
obj014	21:52:00.341	+06:25:22.46	0.332	OII, OIII, H $_{\alpha}$
obj015	21:52:01.092	+06:25:16.26	0.824	OII, OIII
obj016	21:52:00.636	+06:25:37.66	0.289	H $_{\alpha}$, NII
obj017	21:51:58.597	+06:25:11.86	0.847	OII?
obj018	21:51:59.818	+06:25:29.66	0.873	OII
obj019	21:52:00.126	+06:25:13.06	0.879	OII, OIII
obj020	21:52:00.234	+06:24:50.86	0.438	OII, OIII, H $_{\beta}$
obj021	21:51:59.630	+06:25:40.46	0.943	OII
obj022	21:52:00.287	+06:25:06.46	0.989	OII
obj023	21:52:02.058	+06:25:40.46	1.013	OII
obj024	21:51:58.436	+06:25:04.46	1.013	OII
obj025	21:52:00.381	+06:25:20.46	1.052	OII
obj026	21:51:59.549	+06:25:39.06	1.053	OII
obj027	21:52:02.380	+06:24:58.06	0.185	OIII, H $_{\beta}$, H $_{\alpha}$, NII
obj028	21:51:58.583	+06:25:34.26	...	8413.87
obj029	21:52:00.904	+06:24:50.26	1.302	OII
obj030	21:52:00.019	+06:25:13.26	1.318	OII
obj031	21:51:59.952	+06:25:15.46	1.318	OII
obj032	21:51:58.355	+06:25:03.06	1.349	OII
obj033	21:51:58.489	+06:24:59.06	...	8757.32
obj034	21:52:02.354	+06:25:15.46	1.362	OII
obj035	21:51:58.355	+06:25:23.66	1.403	OII
obj036	21:52:00.435	+06:25:13.46	1.430	OII
obj037	21:52:00.623	+06:25:15.86	1.430	OII
obj038	21:52:01.629	+06:25:24.06	1.431	OII
obj039	21:52:00.972	+06:25:33.06	1.433	OII
obj040	21:52:00.703	+06:25:43.06	1.435	OII
obj041	21:52:00.180	+06:25:41.26	1.432	OII
obj042	21:52:00.623	+06:25:15.66	1.430	OII